AIAA SciTech Forum
23-27 January 2023, National Harbor, MD & Online
AIAA SCITECH 2023 Forum

10.2514/6.2023-1043

A High-Order Finite-Difference Method for Linear Stability Analysis and Bi-orthogonal Decomposition of Hypersonic Boundary Layer Flow

Zihao Zou* and Xiaolin Zhong†
University of California, Los Angeles, California, 90095, USA

In the stability analysis of hypersonic flow, modal analysis theories such as the linear stability theory (LST) and bi-orthogonal decomposition play an important role in the instability characteristic analysis including receptivity and linear growth. The essence of this modal analysis lies in the mode decomposition into discrete modes S and F as well as the continuous spectrum, including acoustic, entropy and vorticity modes. Currently, numerical methods used in such analysis involving linear stability theory and multimode decomposition are shooting method or finite difference and spectral collocation methods. The linear stability theory approach used by Malik (1990) deploys fourth-order finite difference and spectral collocation methods to solve a boundary value problem for LST. However, Malik's method is on the computation of discrete modes only. In order to obtain the continuous spectrum for his multimode decomposition frame work, Tumin (2007) relies on a shooting method based on the Runge Kutta scheme with the Gram-Schmidt orthonormalization. However, the Gram-Schmidt orthonormalization is required at every step of the integration in order to minimize the accumulation of numerical errors. To overcome the drawbacks of the two approaches, this paper introduces a general very high-order finite difference method for obtaining the discrete and continuous modes eigenfunctions based on a non-uniform grid method proposed by Zhong and Tatineni (2003). Under the finite difference framework, both discrete and continuous modes can be obtained by imposing proper freestream boundary conditions, including a far field extrapolation boundary condition and the asymptotic boundary condition, which is based on the freestream fundamental solutions. The far field extrapolation boundary condition is efficient and able to solve to both discrete and continuous acoustic modes which have distinct eigenvalues. In addition, the asymptotic boundary condition is used for obtaining continuous modes that have both distinct (acoustic) and similar (vorticity and entropy) eigenvalues. The finite difference method can be applied in various stability analysis for hypersonic flow such as LST, e^N method, and bi-orthogonal decomposition of DNS result in receptivity computation. Extensive verification of the new method has been carried out by comparing the computed discrete and continuous modes as well as the bi-orthogonal decomposition with a supersonic boundary layer flow over a flat plate by comparing with the results from Malik, Tumin, and Miselis (2016). Subsequently, the new method has been applied to a case of freestream receptivity simulation for an axis-symmetric hypersonic flow over a blunt nose cone studied by He and Zhong (2022) and modal contributions are computed by the new method as coefficients to be used in the receptivity analysis.

I. Introduction

Boundary layer transition has always been a critical topic of study in the field of fluid mechanics. The ability to predict and delay the boundary layer transition from laminar to turbulence is desirable in many applications including the design of hypersonic vehicles. For example, the turbulent boundary layer can cause a higher aerodynamic drag and heating on a hypersonic vehicle [1]. To understand the transition behavior and maintain laminar flow, the study of stability of the boundary layer is divided into various paths depending on the disturbance, depicted by Morkovin [2]. In this paper, the main focus is on the small initial disturbances regime. Due to a small perturbation, the disturbed flow will experience the path of receptivity, linear model growth, and nonlinear interaction breakdown leading to instability. During the receptivity process, a freestream pressure or vorticity disturbance enters boundary layer and generates the

*Ph.D. Student, Mechanical and Aerospace Engineering, zzou1@ucla.edu, AIAA Student Member.
†Professor, Mechanical and Aerospace Engineering, xiaolin@seas.ucla.edu, AIAA Associate Fellow.

initial perturbations [3]. These weak initial disturbances will experience a path of linear growth which builds up to nonlinear interaction and energy exchange of modes [4]. The process of analyzing linear growth is often referred as the linear stability theory (LST). Assuming the flow quantities to be composed of the quantity and the weak disturbance, the Navier-Stokes equations can be linearized and decomposed into different modes for analysis. In LST, two groups of problems are being focused on, the temporal and spatial problems. The temporal problem refers to the amplitude of the disturbance changing in time, where the complex frequency has to be determined, while the spatial problem refers to the amplitude changing with the location x, where the search focuses on the complex wave number. The solutions for these two types of problems, temporal and spatial, are proven to contain a sum of discrete modes and continuous modes by Salwen and Grosch [5], and Tumin and Fedorov [6].

Here, the discrete and continuous modes are eigenmodes of different eigenvalues to the linear stability problem. The discrete modes refer to the different normal modes computed by Mack [7] via LST. For example, the first mode refers to the downstream growth of the Tollmien-Schlichting (T-S) waves. Moreover, the second mode and higher order modes discovered by Mack [7] (also called the "Mack modes" or mode S/F defined by Fedorov and Tumin [8]) belong to a family of acoustic waves bouncing between the sonic point, where the velocity is equal to the difference between the phase speed and the local speed of sound, and the wall as depicted by Fedorov [9]. In addition to discrete modes, Mack [10] also investigated the possibility of the existence of a continuous spectrum of eigenvalues by using a plane Poiseuille flow as a guide and moved the upper plane to infinity. His calculations suggested that in addition to a finite number of discrete modes, the discrete spectrum is supplemented by a continuous spectrum of eigenvalues which lies along the phase velocity $c_r = 1$.

Continuing the investigation on the continuous modes, Salwen and Grosch [11] proved that for an unbounded domain like the Blasius flow, the Orr Sommerfield equation could require a integration over a continuum in addition to discrete modes to form a complete set of solution. They also proved the existence of a continuous spectrum by relaxing the freestream boundary condition of the perturbations to be bounded instead of zero. In other words, the continuous modes are not confined within the boundary layer but penetrates out to the freestream. From this result, Salwen and Grosch [5] continued to investigate and showed that the set of discrete and continuous modes of the temporal problem is complete. Hence, an expansion to the sum of discrete and continuous modes is needed to fully describe the temporal problem.

For the spatial problem, Zhigulev, Sidorenko and Tumin [12] found that in the continuous spectrum of the incompressible Orr-Sommerfeld equations, two branches have upstream decaying modes which corresponded to a large growth rate in the downstream. Similarly, for the two dimensional compressible spatial problem of two dimensional perturbations, Tumin and Fedorov [6] had found seven branches in the continuous spectrum with three upstream decaying branches. This result suggested an ill-posedness situation of the spatial problem. To deal with this problem, Tumin and Fedorov also suggested a solution with a finite growth rate (bounded in the downstream solution) and showed that the remaining four branches formed a complete set of solutions combining with the sum of discrete modes. Therefore, a description to the spatial problem also includes both discrete and continuous modes. These continuous modes include a branch of continuous fast acoustic wave which propagates at a relative phase speed of $1 + 1/M$ (where the discrete fast mode originates), a branch of continuous slow acoustic wave at a relative phase speed of $1 - 1/M$ (where the discrete slow mode or the "Mack modes" originates), and two branches of entropy and vorticity waves which have the same phase velocity $c_r = 1$ as the meanflow.

To obtain these discrete and continuous modes numerically, two approaches are widely adopted, an integration-based shooting method and a boundary value problem method. Mack used an integration-based shooting method with the Gram-Schmidt orthonormalization to integrate the inviscid solution from the freestream to the wall to obtain his discrete "Mack" modes. The same method is described by Scott and Watt [13] in detail. Although the use of integration can be computational efficient, this method requires a cumbersome orthonormalization procedure at each step to minimize the numerical parasitic errors. A recovery process is also needed to scale the eigenfunctions properly. In addition, due to the non-linearity of the spatial problem, mainly in the $\frac{\partial^2}{\partial x^2}$ terms, Newton's method is deployed in the iteration to match the boundary condition at the wall. Contrary to Mack, Malik [14] had formulated the spatial LST problem as a boundary value problem and separated the task into a global and local problem due to the non-linearity in the formulation of the spatial problem. The global method is an eigendecomposition on the discrete LST operator assuming a linear relationship for the spatial eigenvalue α. With this assumption, the global method can closely approximate the whole spectrum of spatial eigenvalues. The local method, similar to Mack, makes use of Newton's method for a nonlinear iteration to converge on an eigenvalue that satisfy the boundary conditions. Malik used a second order (global eigenvalue decomposition) and fourth order (local eigenvalue iteration) finite difference method as well as a spectral collocation method to perform the same task. While the spectral collocation has high-order of accuracy, the linear operator is densely populated. This LST method has also been used widely in parallel with direct numerical

simulations (DNS) to investigate disturbance behaviors in hypersonic flow [15], [16],[17]. In these studies, the LST is used as a direct comparison to the unsteady DNS result that is decomposed into a spectrum of discrete frequencies using the Fourier transform. However, Malik focused on the computation of discrete modes and the uses of the LST as a comparison only looked into the unstable discrete modes.

However, as mentioned above, the solution to the stability problem also contains the continuous branches. Furthermore, Balakumar and Malik [18] also concluded that the flow field near a harmonic point source disturbance is mainly represented by the continuous spectrum and few least stable discrete mode. Hence, obtaining the continuous modes is crucial to the stability analysis. Following Mack, Tumin [19] also ultilized the integration-based shooting method to obtain the discrete and continuous eigenfunctions by integrating the freestream eigenfunction solutions to the wall in a two dimensional incompressible boundary layer flow with a two dimensional disturbance. Since the integration is for a wall normal profile, this method is a local method that obtains the eigenmodes individually.

In addition to obtaining the eigenfunctions, Tumin also developed a bi-orthogonal eigenfunction system (BES) using the bi-orthogonality condition first described by Salwen and Grosch [5]. This bi-orthogonal eigenfunction system introduces an adjoint formulation of the direct LST problem which works with the direct eigenfunctions to isolate influences of a single mode. With the introduction of the bi-orthogonal eigenfunction system, one can decompose the unsteady DNS flow field into a combination of different eigenmodes for better understanding of the physics behind. This is called the bi-orthogonal modal decomposition and it can be applied to both temporal and spatial problems allowing the decomposition of a disturbance to known modes. Later, Gaydos and Tumin also studied a two dimensional compressible case with two dimensional disturbance [20]. In addition, Tumin considered a three dimensional disturbance on a two dimensional compressible boundary layer [21] and developed the BES for the two dimensional compressible boundary layer problem as well.

Furthermore, the bi-orthogonal decomposition is particularly useful in the freestream receptivity study of hypersonic flow over a blunt body for a better understanding of the dominant source of the disturbance. Various transition prediction tools such as e^N method and the amplitude method by Mack [22] relies on an accurate initial disturbance amplitude, or so called receptivity coefficient, to predict the transition location. Currently, the receptivity coefficient is obtained either empirically such as in Marineau's work [23] or using a combination of LST and DNS result suggested by Yuet and Zhong [24]. The computational approach for obtaining the receptivity coefficient is an approximated approach that obtains the initial amplitude by dividing the disturbance amplitude at a later location where the unstable mode is dominant with the N factor growth rate of the unstable mode [16]. This reverse technique works since only the second mode will be present at the downstream second mode dominant region and the calculated receptivity coefficient, as a result, is for the second mode. Yet, the initial perturbation at the branch I neutral stability point, where the instability starts on the neutral curve, is composed of weak perturbations from different modes. Using discrete and continuous modes computed by the new method, the modal decomposition of the initial perturbation can be applied easily to obtain the modal receptivity coefficients. Following Tumin's work, the BES including discrete and continuous modes has been a well used tool in the receptivity study of various flow conditions [25],[26] and geometries [27], [28]. Saikia et al. [26] used the BES to examine the amplification of the supersonic discrete mode of a high enthalpy flow over a flat plate. Hasnine et al. [25] studied a particulate induced disturbance over a plate boundary layer of a high speed flow. Tumin et al. [27] and Miselis [28] applied the BES for a freestream hotspot receptivity study of hypersonic flow over a wedge geometries for the consideration of weakly non parallel flow. A survey of applications to receptivity problem in computational and experimental work can also be found in reference [29].

Based on the two methodology reviews above, various drawbacks exist in both numerical approaches. The deficiencies for the integration based shooting method include the locality of the method and the Gram-Schmidt orthonormailization at each step, which also requires a complicated recovery process to scale the coefficient at each step after the integration. The locality of the method requires an accurate initial guess to converge the discrete mode eigenvalues. Both the cumbersome orthonormalization and recovery process can be error prone in the implementation especially in the complex domain. Furthermore, higher-order numerical integration schemes also requires more evaluations of sub-steps. On the other hand, the boundary value problem approach by Malik, which include a global and local method and can be implemented without orthonormalization, only computes the discrete modes.

Moreover, input-output or resolvent analysis is another popular tool recently for transition analysis. In the input-output approach, the Navier-Stokes equations are discretized, using spectral collocation method [30], [31], finite volume method [32] or a numerical Jacobian method by extracting the linear operator from known solvers [33] [34]. An arbitrary forcing, including the nonlinear term from the full nonlinear Navier-Stokes equation [30] [35] or an external forcing on the linearized Navier-Stokes equations [31] [32] [33], acts as the input to the discrete operator and the response of the forcing is studied. Although this analysis accounts for the non-modal effects, both full singular value decomposition

(SVD) of the resolvent operator and the popular power iteration method only decomposes disturbances into modes with respect to the energy norm presented by Chu [36]. This can be less informative than the bi-orthogonal decomposition which decomposes the perturbed flow field into modes according to physical interpretation including acoustic, entropy and vorticity modes. Moreover, with contributions of different modes known, non-modal effects can also be accounted for in the bi-orthogonal eigenfunction decomposition.

Hence, the boundary value problem approach, specifically using the finite difference method, can be examined again in the generation of the continuous spectrum for the bi-orthogonal decomposition. The use of high-order finite difference schemes for boundary layer stability can be found in various direct numerical simulation (DNS) studies. For exmaple, Zhong [37] developed high-order (up to 16th-order) finite difference schemes with non-uniform grid direct discretization for the computation of compressible boundary layer flow based on the full nonlinear Navier-Stokes equations. A more extensive presentation of the family of high-order finite difference schemes can be found in Zhong and Tatineni [38]. Shukla, Tatineni, and Zhong [39] later extended the use of these finite difference schemes in the incompressible flow regime. In addition to the use of finite difference schemes in DNS, Mortensen and Zhong [40] used the Lagrange polynomials to develop a high-order finite difference method in the extension of Malik's LST formulation [14] for the discrete modes. The extension of finite difference method in obtaining the continuous modes is discussed in this work.

In this work, the goal is to develop a new method for multimode decomposition obtaining both discrete and continuous modes using very high-order finite difference on a non-uniform grid with multi-zone. The first part presents the governing equations and the formulation of the spatial problem. The finite difference numerical method is then formulated for obtaining both the discrete and the continuous modes. The very high-order finite difference scheme on a non-uniform grid allows the direct discretization of the linearized Navier-Stokes in the multidomain grid distribution with high-order accuracy and sparse structure. Different boundary conditions are applied in formulating the finite difference solver. With the far field extrapolation boundary condition solving for the disturbance variables directly and the asymptotic boundary condition based on the freestream fundamental solutions, the complete set of discrete and continuous spectrum can be obtained.

The new high-order method is verified by comparing the computed discrete and continuous modes with various cases of supersonic flow over a flat plate from Tumin [21] and Miselis [28]. The bi-orthogonal decomposition for the flat plate case is performed to demonstrate the bi-orthogonal relationship. Furthermore, the bi-orthogonal eigenfunction system result is presented for a Mach 9.81 hypersonic flow over a 5.08 *mm* nose radius blunt cone from He and Zhong [16]. Finally, the bi-orthogonal decomposition is applied on the unsteady DNS flow field of a freestream receptivity simulation for the same flow to obtain the contribution amplitude of each mode including discrete and continuous modes for future receptivity coefficient calculation.

II. Governing Equations

A. Navier-Stokes equations

The Navier-Stokes equations for a viscous compressible flow of ideal gas in Cartesian Coordinates are

$$\frac{\partial \rho^*}{\partial t^*} = \nabla^* \cdot (\rho^* \mathbf{u}^*) = 0 \tag{1}$$

$$\rho^* \left[\frac{\partial \mathbf{u}^*}{\partial t^*} + (\mathbf{u}^* \cdot \nabla^*) \mathbf{u}^* \right] = -\nabla^* p^* + \nabla^* \cdot \left[\lambda^* (\nabla^* \cdot u^*) \mathbf{I} + \mu^* \left(\nabla^* \mathbf{u}^* + \nabla^* \mathbf{u}^{*T} \right) \right] \tag{2}$$

$$\rho^* c_p^* \left[\frac{\partial T^*}{\partial t^*} + (\mathbf{u}^* \cdot \nabla^*) T^* \right] = -\nabla^* \cdot (\kappa^* \nabla^* T^*) + \frac{\partial p^*}{\partial t^*} + \mathbf{u}^* \cdot \nabla^* p^* + \Phi^* \tag{3}$$

where viscous dissipation function is

$$\Phi^* = \lambda^* (\nabla^* \cdot \mathbf{u}^*)^2 + \frac{\mu^*}{2} \left[\nabla^* \mathbf{u}^* + \nabla^* \mathbf{u}^{*T} \right]^2 . \tag{4}$$

The ideal gas law is expressed as

$$p^* = \rho^* R^* T^* . \tag{5}$$

In the above equations, the asterisk, $*$, represents the dimensional form of the variables. The coefficients, c_p is the specific heat and κ is the heat conductivity. We also make use of the Stokes' hypothesis of $\lambda^* = -2\mu^*/3$. The viscosity μ is given by the Sutherland formula.

$$\mu = \mu_{ref}\left(\frac{T}{T_{ref}}\right)^{3/2}\frac{T_{ref}+S_\mu}{T+S_\mu}. \tag{6}$$

The thermal conductivity k is also formulated by the Sutherland formula with the Sutherland temperature S_k.

B. Compressible Linear Stability Equations

From the Navie-Stokes equations, we can derive the stability equations by assuming a small disturbance added on to the quantities.

$$\begin{aligned} &u = \bar{U}+\tilde{u}, \quad v = \bar{V}+\tilde{v}, \quad w = \bar{W}+\tilde{w} \\ &p = \bar{P}+\tilde{p}, \quad \tau = \bar{T}+\widetilde{\theta}, \quad \rho = \bar{\rho}+\tilde{\rho} \\ &\mu = \bar{\mu}+\tilde{\mu}. \end{aligned} \tag{7}$$

Here, the "bar" quantities represent the mean variables and the "bar" symbol is dropped in the following formulation. All flow variables are scaled by their corresponding boundary layer edge values and a reference length scale L is assumed. By applying the local parallel flow assumption and subtracting the base flow equations, we can obtain the non-dimensional linear stability equations.

$$\begin{aligned} \frac{1}{T}\left(\frac{\partial\widetilde{u}}{\partial t}+U\frac{\partial\widetilde{u}}{\partial x}+\widetilde{v}\frac{dU}{dy}+W\frac{\partial\widetilde{u}}{\partial z}\right) = &-\frac{\partial\widetilde{p}}{\partial x}+\frac{\mu}{Re}\left[l_2\frac{\partial^2\widetilde{u}}{\partial x^2}+l_1\left(\frac{\partial^2\widetilde{v}}{\partial x\partial y}+\frac{\partial^2\widetilde{w}}{\partial x\partial z}\right)\right. \\ &+\frac{\partial^2\widetilde{u}}{\partial y^2}+\frac{\partial^2\widetilde{u}}{\partial z^2}+\frac{1}{\mu}\frac{d\mu}{dT}\frac{dT}{dy}\left(\frac{\partial\widetilde{u}}{\partial y}+\frac{\partial\widetilde{v}}{\partial x}\right) \\ &\left.+\frac{1}{\mu}\frac{d\mu}{dT}\left(\frac{\partial^2U}{\partial y^2}\widetilde{\theta}+\frac{dU}{dy}\frac{\partial\widetilde{\theta}}{\partial y}\right)+\frac{1}{\mu}\frac{d^2\mu}{dT^2}\frac{dT}{dy}\frac{dU}{dy}\widetilde{\theta}\right] \end{aligned} \tag{8}$$

$$\begin{aligned} \frac{1}{T}\left(\frac{\partial\widetilde{v}}{\partial t}+U\frac{\partial\widetilde{v}}{\partial x}+W\frac{\partial\widetilde{v}}{\partial z}\right) = &-\frac{\partial\widetilde{p}}{\partial y}+\frac{\mu}{Re}\left[\frac{\partial^2\widetilde{v}}{\partial x^2}+l_1\left(\frac{\partial^2\widetilde{u}}{\partial x\partial y}+\frac{\partial^2\widetilde{w}}{\partial x\partial z}\right)+l_2\frac{\partial^2\widetilde{v}}{\partial y^2}\right. \\ &+\frac{\partial^2\widetilde{v}}{\partial z^2}+\frac{1}{\mu}\frac{d\mu}{dT}\left(\frac{\partial\tilde{\theta}}{\partial x}\frac{dU}{dy}+\frac{\partial\widetilde{\theta}}{\partial z}\frac{dW}{dy}\right) \\ &\left.+\frac{1}{\mu}\frac{d\mu}{dT}\frac{dT}{dy}\left\{l_0\left(\frac{\partial\tilde{u}}{\partial x}+\frac{\partial\widetilde{w}}{\partial z}\right)+l_2\frac{\partial\widetilde{v}}{\partial y}\right\}\right] \end{aligned} \tag{9}$$

$$\begin{aligned} \frac{1}{T}\left(\frac{\partial\widetilde{w}}{\partial t}+U\frac{\partial\widetilde{w}}{\partial x}+\widetilde{v}\frac{dW}{dy}+W\frac{\partial\widetilde{w}}{\partial z}\right) = &-\frac{\partial\widetilde{p}}{\partial z}+\frac{\mu}{\mathrm{Re}}\left[\frac{\partial^2\widetilde{w}}{\partial x^2}+l_1\left(\frac{\partial^2\widetilde{u}}{\partial x\partial z}+\frac{\partial^2\widetilde{v}}{\partial y\partial z}\right)\right. \\ &+\frac{\partial^2\tilde{w}}{\partial y^2}+l_2\frac{\partial^2\tilde{w}}{\partial z^2}+\frac{1}{\mu}\frac{d\mu}{dT}\frac{dT}{dy}\left(\frac{\partial\widetilde{v}}{\partial z}+\frac{\partial\widetilde{u}}{\partial y}\right) \\ &\left.+\frac{1}{\mu}\frac{d\mu}{dT}\left(\frac{d^2W}{dy^2}\widetilde{\theta}+\frac{dW}{dy}\frac{\partial\widetilde{\theta}}{\partial y}\right)+\frac{1}{\mu}\frac{d^2\mu}{dT^2}\frac{dT}{dy}\frac{dW}{dy}\widetilde{\theta}\right] \end{aligned} \tag{10}$$

$$\begin{aligned} &\frac{\gamma M_\infty^2}{T}\frac{\partial\widetilde{p}}{\partial t}-\frac{1}{T^2}\frac{\partial\widetilde{\theta}}{\partial t}+\frac{1}{T}\frac{\partial\widetilde{u}}{\partial x}+U\left(\frac{\gamma M_\infty^2}{T}\frac{\partial\widetilde{p}}{\partial x}-\frac{1}{T^2}\frac{\partial\widetilde{\theta}}{\partial x}\right) \\ &\frac{1}{T}\frac{\partial\widetilde{u}}{\partial y}-\frac{1}{T^2}\frac{\partial\widetilde{\theta}}{\partial y}\widetilde{v}+\frac{1}{T}\frac{\partial\widetilde{w}}{\partial z}+W\left(\frac{\gamma M_\infty^2}{T}\frac{\partial\widetilde{p}}{\partial z}-\frac{1}{T^2}\frac{\partial\widetilde{\theta}}{\partial z}\right)=0 \end{aligned} \tag{11}$$

$$
\begin{aligned}
\frac{1}{T}\left(\frac{\partial\widetilde{\theta}}{\partial t}+U\frac{\partial\widetilde{\theta}}{\partial x}+\widetilde{v}\frac{\partial\widetilde{\theta}}{\partial y}+W\frac{\partial\widetilde{\theta}}{\partial z}\right) &= (\gamma-1)M_\infty^2\left[\frac{\partial\tilde{p}}{\partial t}+U\frac{\partial\widetilde{p}}{\partial x}+W\frac{\partial\tilde{p}}{\partial z}\right] \\
&\quad+\frac{\mu}{RePr}\left[\frac{\partial^2\tilde{\theta}}{\partial x^2}+\frac{\partial^2\widetilde{\theta}}{\partial y^2}+\frac{\partial^2\widetilde{\theta}}{\partial z^2}\right] \\
&\quad+(\gamma-1)M_\infty^2\frac{\mu}{Re}\left[2\frac{dU}{dy}\left(\frac{\partial\widetilde{u}}{\partial y}+\frac{\partial\tilde{v}}{\partial x}\right)\right. \\
&\quad\left.2\frac{dW}{dy}\left(\frac{\partial\tilde{w}}{\partial y}+\frac{\partial\tilde{v}}{\partial z}\right)+\frac{1}{\mu}\frac{d\mu}{dT}\left(\left(\frac{dU}{dy}\right)^2+\left(\frac{dW}{dy}\right)^2\right)\right]
\end{aligned}
\tag{12}
$$

where $l_j = j - \lambda/\mu$. With the above assumption of small perturbations, the higher order terms after the substitution can be dropped. Hence, the governing equations are linearized. For a flat plate profile, the assumption of $dP/dy \to 0$ causes the pressure profile to be constant, $P = 1/\gamma M^2$. For meanflow profiles of other geometry, as suggested by Miselis [28], the assumption is not applicable and the meanflow pressure distribution has to be accounted for in the linearized equations. Moreover, the meanflow temperature boundary condition can be adiabatic or heat transfer at the wall while the fluctuation temperature boundary condition is set to be zero on the wall. This is under an assumption due to the small disturbance and thermal inertia of the wall.

C. Spatial Cauchy Problem

1. Direct Problem

Following Ref. [21], a three dimensional spatially growing perturbation is considered in a boundary layer flow. From the above linearized Navier-Stokes equations, we can assume a periodic-in-time perturbation which leads a solution as $\exp(-i\omega t)$ after a Fourier transformation in time is performed. Following Tumin [21], we can rewrite the linearized Navier-Stokes system in the following form,

$$
\frac{\partial}{\partial y}\left(\mathbf{L}_0\frac{\partial\mathbf{A}}{\partial y}\right)+\mathbf{L}_1\frac{\partial\mathbf{A}}{\partial y}=\mathbf{H}_1A+\mathbf{H}_2\frac{\partial\mathbf{A}}{\partial x}+\mathbf{H}_3\frac{\partial\mathbf{A}}{\partial z}+\mathbf{F} \tag{13}
$$

where $\mathbf{L}_0$, $\mathbf{L}_1$,$\mathbf{H}_1$, $\mathbf{H}_2$, and $\mathbf{H}_3$ are 16 by 16 matrices of coefficients and A is a column vector with 16 components,

$$
\begin{aligned}
\mathbf{A}(x,y,z) =&(u,\partial u/\partial y,v,\pi,\theta,\partial\theta/\partial y,w,\partial w/\partial y,\partial u/\partial x,\partial v/\partial x \\
&\partial\theta/\partial x,\partial w/\partial x,\partial u/\partial z,\partial v/\partial z,\partial\theta/\partial z,\partial w/\partial z)^T.
\end{aligned}
\tag{14}
$$

F above denotes the initial data of $\mathbf{H}_2\mathbf{A}_0$ at $x = 0$. To analyze the spatial growth rate, we apply a Laplace transform in the x direction and Fourier transform in the z direction assuming spanwise periodic perturbation.

$$
\mathbf{A}_{\alpha\beta}=\int_0^\infty e^{-\mathrm{i}\alpha x}\int_{-\infty}^{\infty}e^{-i\beta z}\mathbf{A}(x,y,z)dzdx, \tag{15}
$$

where α is the spatial eigenvalue of interest. After the transformations, the system can be written as

$$
\begin{aligned}
\frac{\partial}{\partial y}\left(\mathbf{L}_0\frac{\partial\mathbf{A}_{\alpha\beta}}{\partial y}\right)+\mathbf{L}_1\frac{\partial\mathbf{A}_{\alpha\beta}}{\partial y} &= \mathbf{H}_1\mathbf{A}_{\alpha\beta}+i\alpha\mathbf{H}_2\mathbf{A}_{\alpha\beta}+i\beta\mathbf{H}_3\mathbf{A}_{\alpha\beta}+\mathbf{H}_2\mathbf{A}_{0\beta} \\
y=0: \quad A_{\alpha\beta_j} &= 0, \quad j=1,3,5,7 \\
y\to\infty: \quad \left|A_{\alpha\beta_j}\right| &< \infty, \quad j=1,\ldots,16.
\end{aligned}
\tag{16}
$$

The elements of $\mathbf{L}_0$, $\mathbf{L}_1$,$\mathbf{H}_1$, $\mathbf{H}_2$, and $\mathbf{H}_3$ are presented in Ref. [21]. The above second-order system of Eq. (16) can be recast as a first-order system of eight components of the following by substituting Eq. (11) into Eq. (9),

$$
\begin{aligned}
\tfrac{d\mathbf{z}_{\alpha\beta}}{dy} &= \mathbf{H}_0\mathbf{z}_{\alpha\beta} \\
y=0: \quad z_{\alpha\beta_j} &= 0, \quad j=1,3,5,7 \\
y\to\infty: \quad \left|z_{\alpha\beta_j}\right| &< \infty, \quad j=1,\ldots,8,
\end{aligned}
\tag{17}
$$

with

$$\mathbf{z}_{\alpha\beta} = (u, \partial u/\partial y, v, \pi, \theta, \partial\theta/\partial y, w, \partial w/\partial y). \tag{18}$$

Here, $\mathbf{H}_0$ is a 8 by 8 coefficient matrix. The elements of $\mathbf{H}_0$ can be found in Appendix A. In the region outside of the boundary layer, the meanflow variables equal to their freestream values, the matrix $\mathbf{H}_0$ is a matrix of constant coefficients. Hence, in the far field, fundamental solutions with an exponential asymptotic behavior $\exp(\lambda y)$ of the homogeneous system can be derived from the characteristic equation,

$$\det\left(\mathbf{H}_0 - \lambda\mathbf{I}\right) = 0. \tag{19}$$

Solving the characteristic equation, we derived the asymptotic solutions $\mathbf{u^0}$ and agreed with Ref. [21]. For the presentation of the asymptotic eigenpairs, refer to Appendix B. Following, let the fundamental solutions to the reduced system in Eq. (17) take the form $\mathbf{U}(y)$ and $\mathbf{U}(y) = [\mathbf{U}_1 \cdots \mathbf{U}_8]$ with the asymptotic values of $\mathbf{u^0}$. Note that the fundamental solutions $\mathbf{U}$ are vectors of 8 components at each y location. We can transform the solutions $\mathbf{U}$ back to the solutions $\mathbf{U}'$ of 16 components by applying the $\frac{\partial}{\partial x}$ and $\frac{\partial}{\partial z}$ in the form of $i\alpha$ and $i\beta$ following Ref. [28]. We then express the solution of the non-homogeneous system of Eq. (16) as following,

$$\mathbf{A}_{\alpha\beta}(y) = \mathbf{U}'\mathbf{Q}(y) + \mathbf{G}(y) \tag{20}$$

where $\mathbf{Q}(y)$ is the set of coefficients to be determined and $\mathbf{G}(y)$ is the non homogeneous part. Note that the sets of $\mathbf{U}'$ and $\mathbf{Q}$ are also functions of $\alpha = f(\lambda)$. To obtain the solutions for Eq. (13) in the Cartesian coordinates, an inverse Laplace transform for the spatial wavenumber α is applied,

$$\mathbf{A}(x, y) = \frac{1}{2\pi\mathrm{i}} \int_{\alpha_0-\infty}^{\alpha_0+\infty} \mathbf{A}_{\alpha\beta}(y; \alpha, \beta) \mathrm{e}^{i\alpha x}\, \mathrm{d}\alpha. \tag{21}$$

Since the complex integration is on the complex α plane, the discrete α values of a sample compressible flow over a flat plate is plotted in Fig.1 to show the integration domain. A discrete representation of the continuous branch cuts is shown since each branch can be describe with the fundamental solution eigenvalues $\lambda^2 = -ik$ for a range of discrete K values from 0 to ∞. Following the integration contour in Ref. [41] on the complex α plane, the integration in Eq. (21) uses a contour around branch cuts and residues, which are characterized as continuous and discrete modes accordingly. For the continuous spectrum, the contour integral path around each branch can be described as a path from ∞ to $K = 0$, where $K = 0$ being the branch point for each branch function of $\lambda^2 = -ik$, subtracting a path from $K = 0$ to ∞. The set of $\mathbf{A}_{\alpha\beta}\mathrm{e}^{\mathrm{i}\alpha x}$ behaves differently as $\alpha = f(\lambda) = f(k)$ goes from 0 to ∞ at each branch and some coefficients $\mathbf{Q}$ for the fundamental solutions in the set $\mathbf{U}'$ cancel out. For the detailed analytical procedure, refer to Ref. [41]. This means that it is sufficient to only consider the remaining fundamental solutions when computing the solution $\mathbf{A}_{\alpha\beta}$ before the inverse Laplace transform. This leads to a combination of different fundamental solutions $\mathbf{U}'_1 \cdots \mathbf{U}'_8$ for each continuous branch. For example, the branch cut corresponding to the acoustic waves is comprised of $\mathbf{U}'_1$, $\mathbf{U}'_3$, $\mathbf{U}'_4$, $\mathbf{U}'_5$, $\mathbf{U}'_7$, which correspond to the following in the 8-component system,

$$z_{\alpha\beta}^{Acoustic} = c^{(1)}\mathbf{U}^{(1)} + c^{(3)}\mathbf{U}^{(3)} + c^{(4)}\mathbf{U}^{(4)} + c^{(5)}\mathbf{U}^{(5)} + c^{(7)}\mathbf{U}^{(7)}. \tag{22}$$

We can refer to Tumin (2007) for all the modes. For the discrete modes, the residue results in the combination of decaying modes $\mathbf{U}'_1$, $\mathbf{U}'_3$, $\mathbf{U}'_5$, $\mathbf{U}'_7$. In practice, we use the fundamental solutions $\mathbf{U}(y)$ of 8 components and solve for the solution $\mathbf{z}_{\alpha\beta}(y)$. In the later section, we will utilize the combinations of fundamental solutions and their asymptotic results as boundary conditions to solve for the continuous modes of the solution for Eq. (17) with a general high-order finite difference method. Details of the numerical method and the application of boundary conditions will be discussed in later sections.

2. Bi-orthogonal Eigenfunction System

Since the solution for Eq. (16) is not self adjoint, a bi-orthogonal eigenfunction system can be introduced with an adjoint system. The adjoint solution acts as a filter for the direct solution and forms an orthogonality relationship between normal modes. We can introduce the general adjoint operator $\mathcal{L}^*$ from the inner product of a general vector $\mathcal{L}\mathcal{A}$ and $\mathcal{B}$.

$$\langle \mathcal{L}\mathcal{A}, \mathcal{B} \rangle = \langle \mathcal{A}, \mathcal{L}^*\mathcal{B} \rangle . \tag{23}$$

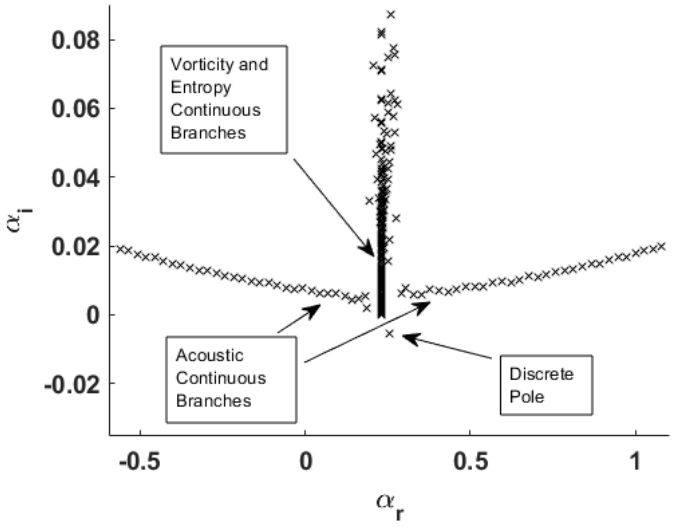

Fig. 1 The global spatial eigenvalue spectrum showing the continuous branch cuts and discrete poles.

Let the operator $\mathcal{L}$ be the linear operator of Eq. (16) and $\mathcal{A} = \mathbf{A}_{\alpha\beta}$, we can introduce the following adjoint system with $\mathbf{B}_{\alpha\beta} = \mathcal{B}*$, where the $*$ denotes the complex conjugate,

$$\begin{gathered}\frac{\partial}{\partial y}\left(\mathbf{L}_0^T\frac{\partial \mathbf{B}_{\alpha\beta}}{\partial y}\right) - \mathbf{L}_1^T\frac{\partial \mathbf{B}_{\alpha\beta}}{\partial y} = \mathbf{H}_1^T\mathbf{B}_{\alpha\beta} + i\alpha\mathbf{H}_2^T\mathbf{B}_{\alpha\beta} + i\beta\mathbf{H}_3^T\mathbf{B}_{\alpha\beta} \\ y = 0: \quad B_{\alpha\beta_j} = 0, \quad j = 2,4,6,8 \\ y \to \infty: \quad \left|B_{\alpha\beta_j}\right| < \infty, \quad j = 1,\ldots,16.\end{gathered} \tag{24}$$

Here, the transpose is the conventional transpose. Similarly, the adjoint system can also be recast in the following form,

$$\begin{gathered}-\tfrac{\mathrm{d}\mathbf{Y}_{\alpha\beta}}{\mathrm{d}y} = H_0^T\mathbf{Y}_{\alpha\beta}. \\ y = 0: \quad Y_{\alpha\beta_j} = 0, \quad j = 2,4,6,8 \\ y \to \infty: \quad \left|Y_{\alpha\beta_j}\right| < \infty, \quad j = 1,\ldots,8\end{gathered} \tag{25}$$

The solution $\mathbf{Y}_{\alpha\beta}$ can also be expressed as a combination of fundamental solutions, $\mathbf{V}_1 \cdots \mathbf{V}_8$, with the freestream fundamental solution vectors, $\mathbf{V}_j^0,\ j = 1,\cdots,8$. The freestream fundamantal solutions for the adjoint problem can be found using cofactors of the matrix of freestream fundamental solution vectors from the direct problem. The transformation between $\mathbf{B}_{\alpha\beta}$ and $\mathbf{Y}_{\alpha\beta}$ can be referred to Tumin [21]. With the dual systems, the orthogonality condition exists as

$$i\left(\alpha - \alpha'\right)\int_0^\infty \left(\mathbf{H}_2\mathbf{A}_{\alpha\beta}, \mathbf{B}_{\alpha'\beta}\right) dy = 0. \tag{26}$$

This orthogonality relation can be obtained by an integration by part of the dot product between $\mathbf{B}_{\alpha'\beta}$ and Eq. (16). The above equation can be rewritten into this form,

$$\left\langle \mathbf{H}_2\mathbf{A}_{\alpha\beta}, \mathbf{B}_{\alpha'\beta}\right\rangle = \int_0^\infty \left(\left(\mathbf{H}_2\mathbf{A}_{\alpha\beta}\right), \mathbf{B}_{\alpha'\beta}\right) dy = \Gamma\Delta_{\alpha\alpha'}. \tag{27}$$

According to Ref. [5], for the discrete modes , the term $\Delta_{\alpha\alpha'}$ represents a Kronecker Delta, which equals to 1 if the eigenvalues of the two modes are the same. This is because the decaying behavior of the discrete modes and the integral should result in a constant Γ value depending on the normalization. For the continuous modes, the same term represents a Dirac Delta. One can also derive the following inner product relation between $\mathbf{A}_{\alpha\beta}$ and $z_{\alpha\beta}$. This would be helpful in the numerical implementation later [21],

$$\left\langle H_2 \boldsymbol{A}_{\alpha\beta}, \boldsymbol{B}_{\alpha\beta} \right\rangle = -\mathrm{i} \left\langle \frac{\partial \boldsymbol{H}_0}{\partial \alpha} z_{\alpha\beta}, \boldsymbol{Y}_{\alpha\beta} \right\rangle. \tag{28}$$

We can obtain the coefficients for each modes using the following relation assuming local parallel flow,

$$C_{mode} = \frac{-\mathrm{i} \left\langle \frac{\partial \boldsymbol{H}_0}{\partial \alpha} z_{DNS}, \boldsymbol{Y}_{\alpha\beta} \right\rangle}{\Gamma}. \tag{29}$$

In practice, the numerical coefficients can be obtained by a numerical integration of the dot product from the wall to the freestream using a composite trapezoidal rule which will be discussed later.

III. Numerical Methods

A. General High-Order Finite Difference Scheme On Non-uniform Grid

Instead of solving the Runge Kutta fourth order integration with orthonormalization, a high-order implicit method can be applied through finite difference. This numerical approximation of the first derivative will be carried out on a non uniform grid to avoid the Runge phenomenon. The distribution of N number of grid points over the domain $[a, b]$ will follow Kosloff [42], Zhong [38], and Shukla [39],

$$y_j = \frac{b+a}{2} + (b-a)\frac{\sin^{-1}(-\alpha \cos(\pi j/N))}{2\sin^{-1}\alpha}, \quad j = 0, \ldots, N, \tag{30}$$

where the parameter α can be tuned to stretch the grid from a uniform grid ($\alpha = 1$) to a Chebyshev grid ($\alpha = 0$). This stretching is tuned such that the discrete operator is stable. Various trends of stable α tuning can be found in Zhong [38]. This direct application of the finite difference method on a non-uniform grid eliminates the grid transformation procedure needed in previous spectral collocation method [14]. Furthermore, a multi domain grid distribution is also applied. Three domains in total are used in the boundary layer. The first domain accounts for half of the total grid points and emphasizes on the critical layer where the maximum temperature gradient is located. This corresponds to the non-dimensional location $0 \leq y_j \leq y_i$ where the location of y_i depends on the meanflow profile. The second domain accounts for the one fourth of the total grid points and ends when the streamwise velocity equals to 90 percent of the freestream velocity. This corresponds to the non-dimensional location $y_i \leq y_j \leq y_o$ where the locations of y_i and y_o depend on the meanflow profile. The third domain covers the rest of the profile, $y_o \leq y_j \leq y_{max}$. With the grid defined, we apply the finite difference method. To derive the finite difference coefficients on an arbitrary stencil of $n+1$ points, we use the Lagrange polynomial.

$$f(x) = \sum_{j=0}^{n} f\left(x_j\right) L_j(x) \tag{31}$$

where

$$L_j(x) = \prod_{i \neq j} \frac{x - x_i}{x_j - x_i} \tag{32}$$

By taking the derivative of the Lagrange polynomial over x, we have

$$L_j'(x) = \sum_{l \neq j} \frac{1}{x_j - x_l} \prod_{m \neq (j,l)} \frac{x - x_m}{x_j - x_m} \tag{33}$$

and the second derivative can be derived in a similar fashion by taking the logarithmic derivative. Hence, we have

$$f'(x) = \sum_{j=0}^{n} f\left(x_j\right) L_j'(x) \tag{34}$$

where $L_j'(x)$ are the finite difference coefficients to the first derivative. With the finite difference coefficients determined, we approximate the first derivative in our linear system from $i = 0, \ldots, N$. Since the vector $\mathbf{z}_{\alpha\beta}$ from Eq. (17) has 8 components, each coefficient for the finite difference scheme is multiplied by an 8 by 8 identity matrix, $\mathbf{I}$.

$$\mathbf{L}'_j(x) = L'_j(x) * \mathbf{I}, \quad i = 0, \ldots, n. \tag{35}$$

Hence, each $\mathbf{L}'_j(x)$ is a block of size 8 by 8. For an arbitrary first order finite difference operator of length $n+1$, we can approximate the first order finite difference part in Eq. (17) at each y_i location as

$$\frac{d\mathbf{z}_{\alpha\beta}(y_i)}{dy_i} = \sum_{j=0}^{n} \mathbf{z}_{\alpha\beta}(y_j)\, \mathbf{L}'_j(y_i), \quad i = 0, \ldots, N. \tag{36}$$

We can rewrite the summation as a banded block linear operator with a bandwidth of $n+1$ and block size of 8 by 8. Combining all the interior points, we result in a banded block operator, $\mathbf{D}$, with N block rows,

$$\frac{d\mathbf{z}_{\alpha\beta}}{dy} = \mathbf{D}\mathbf{z}_{\alpha\beta}, \tag{37}$$

where

$$[\mathbf{D}] = \begin{bmatrix} [\mathbf{L}'_0] & \cdots & [\mathbf{L}'_n] & 0 & \cdots & 0 \\ 0 & [\mathbf{L}'_0] & \cdots & [\mathbf{L}'_n] & \cdots & 0 \\ 0 & 0 & \ddots & \ddots & & 0 \\ 0 & \cdots & [\mathbf{L}'_0] & \cdots & [\mathbf{L}'_n] & 0 \\ 0 & \cdots & 0 & [\mathbf{L}'_0] & \cdots & [\mathbf{L}'_n] \end{bmatrix} \tag{38}$$

We can also formulate the right hand side of Eq. (17) as a block diagonal operator, $\mathbf{H}$. The 8 by 8 matrix $\mathbf{H_0}$ will be a diagonal block for each y_i location from $i = 0$ to N.

$$[\mathbf{H}] = \begin{bmatrix} [\mathbf{H_0}(y_0)] & 0 & 0 & 0 & \cdots & 0 \\ 0 & [\mathbf{H_0}(y_1)] & 0 & 0 & \cdots & 0 \\ 0 & 0 & \ddots & \ddots & & 0 \\ 0 & \cdots & 0 & 0 & [\mathbf{H_0}(y_{N-2})] & 0 \\ 0 & \cdots & 0 & 0 & 0 & [\mathbf{H_0}(y_N)] \end{bmatrix} \tag{39}$$

Substituting the discrete operators into Eq. (17) and subtracting the $\mathbf{H}$ operator from both side, we obtain the following equation.

$$\mathbf{D}\mathbf{z}_{\alpha\beta} - \mathbf{H}\mathbf{z}_{\alpha\beta} = 0 \tag{40}$$

Both $\mathbf{D}$ and $\mathbf{H}$ are block banded matrices of size $N * 8$ by $N * 8$. For the boundary treatments, one sided difference scheme derived from the same method is implemented on both ends. For the wall boundary block row, the one sided difference with a stencil length of n points gives

$$\left([\mathbf{L}'_0] - [\mathbf{H}_0(y_0)]\right) \begin{bmatrix} u(y=0) \\ du/dy(y=0) \\ v(y=0) \\ p(y=0) \\ \theta(y=0) \\ d\theta/dy(y=0) \\ w(y=0) \\ dw/dy(y=0) \end{bmatrix} + \cdots + [\mathbf{L}'_n] \begin{bmatrix} u(y_n) \\ du/dy(y_n) \\ v(y_n) \\ p(y_n) \\ \theta(y_1) \\ d\theta/dy(y_n) \\ w(y_n) \\ dw/dy(y_n) \end{bmatrix} + 0 + \cdots + 0 = [0], \tag{41}$$

and similarly for the freestream boundary block row,

$$0 + \cdots + 0 + [\mathbf{L}_0'] \begin{bmatrix} u(y_{N-n}) \\ du/dy(y_{N-n}) \\ v(y_{N-n}) \\ p(y_{N-n}) \\ \theta(y_{N-n}) \\ d\theta/dy(y_{N-n}) \\ w(y_{N-n}) \\ dw/dy(y_{N-n}) \end{bmatrix} + \cdots + \left([\mathbf{L}_n' - [\mathbf{H}_0(y_N)]\right) \begin{bmatrix} u(y_N) \\ du/dy(y_N) \\ v(y_N) \\ p(y_N) \\ \theta(y_N) \\ d\theta/dy(y_N) \\ w(y_N) \\ dw/dy(y_N) \end{bmatrix} = [0], \tag{42}$$

Matrix $\mathbf{H}$ can be split into three parts: $\bar{\mathbf{H}}$ is the part that does not depend on the spatial wavenumber α, $\dot{\mathbf{H}}$ is linearly dependent on α, and $\ddot{\mathbf{H}}$ is dependent on α^2. Along with boundary conditions from Eq. (17), Eq. (40) can be written as

$$\begin{gathered} \left(\mathbf{D} - \left(\bar{\mathbf{H}} + \alpha\dot{\mathbf{H}} + \alpha^2\ddot{\mathbf{H}}\right)\right)\mathbf{z}_{\alpha\beta} = 0 \\ z_{\alpha\beta_j} = 0, \quad j = 1, 3, 5, 7 \\ \left|z_{\alpha\beta_j}\right| < \infty, \quad j = N*8, \ldots, N*8-7. \end{gathered} \tag{43}$$

The problem can then be described as a set of linear equations taking form in $[\mathbf{A}][\mathbf{x}] = [\mathbf{b}]$, where $[\mathbf{A}] = [\mathbf{D} - (\bar{\mathbf{H}} + \alpha\dot{\mathbf{H}} + \alpha^2\ddot{\mathbf{H}})]$, $[\mathbf{x}] = [\mathbf{z}_{\alpha\beta}]$, and $[\mathbf{b}] = 0$. Note that Eq. (43) has a nonlinear dependence on the spatial wavenumber α. If the nonlinear term is omitted or α^2 is set to 0, a global eigenvalue decomposition can be performed as the global method presented in Ref. [14]. Furthermore, at the boundary of each domain inside the boundary layer profile, we have to ensure continuity. Following Malik [14], this can be done by enforcing the perturbation variables and their derivatives to be equal at the end of zones. For example, at yi,

$$\mathbf{z}^I_{\alpha\beta}(y_i) = \mathbf{z}^{II}_{\alpha\beta}(y_i) \tag{44}$$

and

$$\frac{d\mathbf{z}_{\alpha\beta}(y_i)^I}{dy_i} = \frac{d\mathbf{z}_{\alpha\beta}(y_i)^{II}}{dy_i}. \tag{45}$$

The discrete adjoint operators can be obtained in the same way. Following Eqs. (25) and (40), the discrete adjoint formula can be written as

$$\begin{gathered} -\mathbf{D}\mathbf{Y}_{\alpha\beta} - \mathbf{H}^T\mathbf{Y}_{\alpha\beta} = 0 \\ Y_{\alpha\beta_j} = 0, \quad j = 2, 4, 6, 8 \\ \left|Y_{\alpha\beta_j}\right| < \infty, \quad j = N*8, \ldots, N*8-7. \end{gathered} \tag{46}$$

1. Discrete Mode Boundary Conditions

From Eq. (43), the problem $[\mathbf{A}][\mathbf{x}] = [\mathbf{b}]$ is singular due to $[\mathbf{b}] = 0$. To avoid this situation, we will make modifications on the wall boundary conditions by normalizing with the wall pressure or the streamwise velocity gradient, $\frac{du(0)}{dy}$, term. For the discrete mode wall boundary, we switch out the 1st, 3rd, and 7th rows of Eq. (41) with equations $u(y=0)$, $v(y=0)$, $w(y=0) = 0$ for the no slip condition. For the 5th row, instead of the temperature boundary condition, $\theta(y=0) = 0$, we normalize by the pressure term such that $p(y=0) = 1$ to address for the singularity. Other rows will remain unchanged. Since Eq. (43) has a nonlinear dependence on α, Newton's method is applied as a nonlinear search for the correct α that meets the temperature boundary condition. Currently, the sparse LU decomposition from MATLAB is used to solve the linear system where the same LU decomposition can be used in the Newton's iteration. More details will follow after the discussion on continuous modes.

The freestream boundary condition $\mathbf{z}_{\alpha\beta N}$ will be zeros since the discrete modes are set to decay. The block row of Eq. (42) can be rewritten as

$$\begin{bmatrix} u(y_N) \\ du/dy(y_N) \\ v(y_N) \\ p(y_N) \\ \theta(y_N) \\ d\theta/dy(y_N) \\ w(y_N) \\ dw/dy(y_N) \end{bmatrix} = [0]. \tag{47}$$

The adjoint wall boundary condition is applied in a similar way except that the spatial wavenumber α is shared between the two systems and is converged by the Newton's method in the direct problem. Hence, the four wall boundary conditions in Eq. (46) can be applied directly. The adjoint decaying freestream boundary condition takes a similar form.

2. Continuous Mode Boundary Conditions

After solving for the discrete modes, the continuous modes can also be obtained with the same framework of Eqs. (43) with different boundary conditions. For the continuous mode, the singularity at the wall can be addressed directly by imposing the no slip condition and the normalization together. The reason behind is that we can determine the spatial eigenvalue of the continuous modes with a priori knowledge of the asymptotic results by setting $\lambda = -K^2$ for λ formulations in Eq. (75). Hence, the nonlinear iteration for an α that satisfy the wall boundary condition is not necessary and we can set the wall boundary conditions and the normalization directly in the linear operator. Since values of ω and β are set in the formulation of λ, different selections of $\lambda = -K^2$ correspond to specific locations of each branch in the complex α plane. The λ relation is a nonlinear relation with respect to α. We deploy another nonlinear solver of Brent's method [43], also used by Miselis [28], to determine the root. To describe the behavior of the whole branch, we discretize K from $K = 0$ to $K = 4$, following Tumin [19], and sum up the contribution for all values of K. Eigenfunctions of each mode will be computed for all discrete values of K in order to represent the integral along the branch.

Furthermore, from the eigenpairs described in the Appendix B, for any eigenvalue of $Re(\lambda) < 0$, a corresponding eigenvalue of $Re(\lambda) > 0$ exists. In order to enforce the boundedness of the freestream boundary condition, $\exp(\lambda_j y_{freestream}) < \infty$, two types of solutions were introduced by Salwen and Grosch [5]. The first type is the discrete solution which decays in the freestream and second is the continuous spectra which is bounded in the freestream. We can describe the boundedness condition with two numerical boundary condition, the far field extrapolation and the asymptotic boundary condition. For the far field extrapolation boundary condition, we utilize an extrapolation using the Lagrange polynomials mentioned above to substitute for freestream perturbation values.

$$\mathbf{z}_{\alpha\beta}\left(y_N\right) = \sum_{j=N-n}^{N-1} \mathbf{z}_{\alpha\beta}\left(y_j\right) L_j(y) \tag{48}$$

where n is the length of the stencil. The same stencil length as the interior scheme can be used for the extrapolation with one order of accuracy lower than the interior scheme since the extrapolation is one sided. Hence, the first order derivative approximation at point N becomes

$$0 + \cdots + 0 + \mathbf{L}'_0 * \mathbf{z}_{\alpha\beta N-n} + \cdots + \mathbf{L}'_n * \left(\sum_{j=N-n}^{N-1} \mathbf{z}_{\alpha\beta}\left(y_j\right) L_j\left(y_j\right) \right) = \frac{d\mathbf{z}_{\alpha\beta}\left(y_N\right)}{dy}. \tag{49}$$

Plugging Eq. (49) into the last block row of the linear operator $\mathbf{D}$ in Eq. (40), we will obtain the full linear operator with a far field extrapolation boundary condition to obtain continuous modes such as fast and slow acoustic modes. For continuous modes such as fast and slow acoustic modes, the eigenvalues are isolated in complex wavenumber plane. Hence, the far field extrapolation boundary condition is sufficient to obtain the isolocated eigenfunctions without non-modal effects. Only the corresponding eigenvalue, which can be solved from the $\lambda = -K^2$ equation for a K value, will be needed to solve the system.

For the entropy and vorticity continuous modes which the eigenvalues are close to each other, the asymptotic boundary condition can by applied using the principle of superposition. From the inverse Laplace transform mentioned

above, the full solution of a continuous branch is made up of a linear combination of fundamental solutions $\mathbf{U}$ from Eq. (20) where $\mathbf{U}(y) \sim \exp(\lambda_j y)$. Hence, we use the asymptotic fundamental solutions with the a priori knowledge of different combinations from the contour integral of Eq. (21). From the result of the contour integral in Ref. [21], the continuous modes are obtained with the combination of five fundamental solutions including freestream decaying and non-decaying fundamental solutions. For example, the vorticity mode A is obtained with the following.

$$\begin{aligned}\mathbf{z}^{VA}_{\alpha\beta} &= c^{(1)}\mathbf{U}^{(1)} + c^{(2)}\mathbf{U}^{(2)} + c^{(3)}\mathbf{U}^{(3)} + c^{(5)}\mathbf{U}^{(5)} + c^{(8)}\mathbf{U}^{(8)} \\ \mathbf{Y}^{VA}_{\alpha\beta} &= c^{(1)}\mathbf{V}^{(1)} + c^{(2)}\mathbf{V}^{(2)} + c^{(4)}\mathbf{V}^{(4)} + c^{(6)}\mathbf{V}^{(6)} + c^{(7)}\mathbf{Y}^{(7)}\end{aligned} \tag{50}$$

with coefficients $\mathbf{c}$ determined to satisfy the wall boundary conditions. For the combination of other modes, we refer to Ref.[21] for the results of the inverse Laplace transformation. Therefore, instead of applying the finite difference stencil to Eq. (17), we apply the finite difference method to the following equations,

$$\frac{d\mathbf{U}^{(j)}\mathbf{c}}{dy} = \mathbf{H}_0\left(\mathbf{U}^{(j)}\mathbf{c}\right), \quad j = 1, \cdots, 5 \tag{51}$$

with j representing each of the 5 fundamental solutions used in the combination to form a specific continuous mode. The freestream fundamental solutions $\mathbf{u}^0$ are used as the freestream boundary condition with a freestream coefficient of $c_{freestream}$ or $c_N = 1$,

$$\mathbf{U}^{(j)}(y = N)c_N = \mathbf{u}^0_{(j)}, \quad j = 1, \cdots, 5. \tag{52}$$

In practice, we treat $\mathbf{U}^{(j)}\mathbf{c}$ as one variable to solve together. Applying the finite difference scheme same as Eq. (40), we will result in an discrete equation for each fundamental solution $\mathbf{Z}$ with its own freestream asymptotic boundary conditions $\mathbf{z}^0$. Hence, a discrete equation similar to Eq. (40) can be formulated,

$$\mathbf{D}\left(\mathbf{U}^{(j)}\mathbf{c}\right) - \mathbf{H}\left(\mathbf{U}^{(j)}\mathbf{c}\right) = 0, \quad j = 1, \cdots, 5. \tag{53}$$

For each continuous mode, we solve for Eq. (53) five times to obtain the five fundamental solutions. Since the linear operator is banded and sparse, solving for the five fundamental solutions can still be cost efficient. For the coefficients $\mathbf{c}$, we first assume an arbitrary scaling of 1 for the coefficient in the freestream, $c_N = 1$, and solve for the $\mathbf{U}^{(j)}_{\alpha\beta}(y)c$ throughout the boundary layer with the finite difference scheme. This is equivalent to normalizing the fundamental solutions with the freestream coefficient,c_N. After solving for the fundamental solutions using the finite difference method, we have the $\mathbf{U}_{wall}\frac{\mathbf{c}_{wall}}{\mathbf{c}_N} = \mathbf{U}_{wall}\mathbf{c}_{\text{old}}$ values at the wall which does not scale to our wall boundary conditions yet. Then we enforce the boundary condition at the wall by solving for the new coefficients, $\mathbf{c}^{new}$, with the following system of algebraic equations,

$$\begin{bmatrix} z_{\alpha\beta 1}(0) \\ z_{\alpha\beta 3}(0) \\ z_{\alpha\beta 5}(0) \\ z_{\alpha\beta 7}(0) \\ z_{\alpha\beta 2,4}(0) \end{bmatrix} = \begin{bmatrix} \vdots & \vdots & \vdots & \vdots & \vdots \\ \mathbf{U}^{(1)}_{\text{wall}}\mathbf{c}_{\text{old}} & \mathbf{U}^{(2)}_{\text{wall}}\mathbf{c}_{\text{old}} & \mathbf{U}^{(3)}_{\text{wall}}\mathbf{c}_{\text{old}} & \mathbf{U}^{(4)}_{\text{wall}}\mathbf{c}_{\text{old}} & \mathbf{U}^{(5)}_{\text{wall}}\mathbf{c}_{\text{old}} \\ \vdots & \vdots & \vdots & \vdots & \vdots \end{bmatrix} \begin{bmatrix} c^{(1)}_{\text{new}} \\ c^{(2)}_{\text{new}} \\ c^{(3)}_{\text{new}} \\ c^{(4)}_{\text{new}} \\ c^{(5)}_{\text{new}} \end{bmatrix}. \tag{54}$$

This is done by setting the $z_{\alpha\beta_1}(0)$, $z_{\alpha\beta_3}(0)$ and $z_{\alpha\beta_7}(0)$ equal to 0 in the equation to satisfy the no slip condition, $z_{\alpha\beta_5}(0) = 0$ for the temperature wall boundary condition. A normalization of the wall pressure fluctuation, $z_{\alpha\beta_4}(0) = 1$, or the streamwise velocity gradient, $z_{\alpha\beta_2}(0) = 1$, is also applied. Since we have five fundamental solutions in each continuous mode, we have five equations to determine the coefficients needed to satisfy the five boundary conditions at the wall. With these conditions, we can determine the scaling that satisfy the wall boundary condition and rescale the fundamental solutions

$$\mathbf{z}_{\alpha\beta} = c^{(1)}_{new}\left(\mathbf{U}^{(1)}\mathbf{c}_{\text{old}}\right) + c^{(2)}_{new}\left(\mathbf{U}^{(2)}\mathbf{c}_{\text{old}}\right) + c^{(3)}_{new}\left(\mathbf{U}^{(3)}\mathbf{c}_{\text{old}}\right) + c^{(4)}_{new}\left(\mathbf{U}^{(4)}\mathbf{c}_{\text{old}}\right) + c^{(5)}_{new}\left(\mathbf{U}^{(5)}\mathbf{c}_{\text{old}}\right). \tag{55}$$

The adjoint freestream fundamental solutions are obtained mathematically by defining the adjoint of the direct freestream fundamental solution following Tumin [21]. In another word, it is defined as the transpose of the cofactor matrix of the matrix of direct freestream fundamental solutions $\mathbf{z}_0$.

B. Newton's iteration

For the discrete modes, each spatial eigenvalue α is converged using the Newton's method to drive the temperature fluctuation at the wall to 0 or the streamwise velocity to 0. As mentioned above, the coefficients at wall are determined by the no slip condition and the normalization of pressure. With a guessed value of α_0, we can apply the finite difference method to solve for the temperature or velocity fluctuation at the wall. For the temperature fluctuation, we have $\theta_{\text{wall}} = z_{\alpha_0\beta_5}(0)$. at $y = 0$, We then take the derivative of the discrete system resulting in the following equation with boundary conditions

$$(\mathbf{D} - \mathbf{H}) \frac{\partial \mathbf{z}_{\alpha\beta}}{\partial \alpha} = \frac{\partial \mathbf{H}}{\partial \alpha} \mathbf{z}_{\alpha\beta} + B.C. \tag{56}$$

where the boundary condition, $B.C.$, does not change with α for the discrete mode case. Note that the finite difference stencil D does not depend on α. By solving this equation, we will be able to obtain $\frac{\partial \theta_{\text{wall}}}{\partial \alpha}$ and apply the Newton's iteration,

$$\alpha_{new} = \alpha_0 - \theta_{wall}^{\alpha_0} \left(\frac{\partial \theta_{\text{wall}}}{\partial \alpha} \right)^{-1}, \tag{57}$$

to get the new spatial eigenvalue. Since we have already LU factorized the matrix $[\mathbf{D} - \mathbf{H}]$ when we solve for the direct system, we can obtain the $\frac{\partial \mathbf{z}_{\alpha\beta}}{\partial \alpha}$ without extra decomposition. Malik [14] also suggested to keep the same LU factorization for a small number of iterations before updating to further save computational cost.

C. Bi-orthogonal Decomposition

After formulating the numerical procedure to obtain both discrete and continuous modes, the bi-orthognality relationship between the direct and adjoint eigenfunctions can be used as a filter to isolate the modal behavior. For the implementation, an inner product between the direct and adjoint eigenfunctions is used in Eqs. (27) and (28). From Eq. (28), we can write

$$\left\langle \frac{\partial \boldsymbol{H}_0}{\partial \alpha} z_{\alpha\beta}, \boldsymbol{Y}_{\alpha\beta} \right\rangle = \int_0^\infty \left(\frac{\partial \boldsymbol{H}_0}{\partial \alpha} z_{\alpha\beta}, \boldsymbol{Y}_{\alpha\beta} \right) dy = \Gamma \Delta_{\alpha\alpha'}. \tag{58}$$

Using a non-uniform trapezoidal rule, the integration can be numerically implemented as the following. Let f be the function of the dot product inside the integral for Eq. (58),

$$\int_0^\infty f dy \approx \sum_{K=1}^{N} \frac{f(y_{k-1}) + f(y_k)}{2} \Delta y_k, \tag{59}$$

where ∞ is approximated at the freestream upper bound y_{max} location of the domain. Hence, from the inner product of the direct and adjoint solutions of the same mode, the normalization value, Γ, can be calculated for both discrete and continuous modes. Note that the normalization is dependent on the normalization boundary conditions mentioned above. A consistent normalization across the modes is necessary. After obtaining Γ, Eq. (29) can be ultilized to compute the amplitude of modal contribution for a perturbed flowfield. Again, the contribution amplitude of a particular mode in a perturbation is computed with an inner product of the perturbed flow field and the corresponding mode's adjoint eigenfunctions with the normalization.

IV. Results

A. Verification of Finite Difference Scheme

In order to study the convergence behavior of the finite difference scheme, a test case using the Bessel function of first kind is solved for its first derivative since the exact derivative can be obtained with the Matlab built in function. The finite difference scheme is used on the zeroth order Bessel function values and the result is compared with the first order Bessel function values. To verify the convergence, test trials are made of a range of different numbers of grid points and stencil length. Figure 2 presents the error behaviors when the various finite difference schemes are applied onto the Bessel function.

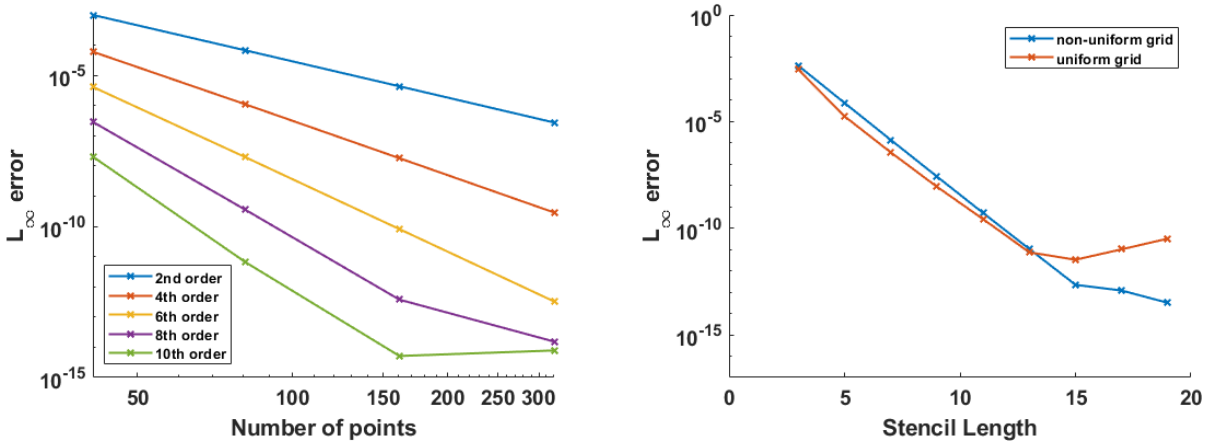

(a) L_∞ **errors for the derivative to the Bessel function.** **(b)** L_∞ **errors for various grid distributions.**

Fig. 2 Order of accuracy verification for the high-order finite difference scheme over a non-uniform grid.

Figure 2a is the infinity norm error versus the number of grid points for different stencils on the non-uniform grid. From Fig.2a, We can see that the error decreases according to the predicted trends and reaches 10^{-14} to 10^{-15}. For the non-uniform grid, we set the number of grid points $N = 101$ and varied the lengths of stencils. The grid tuning parameter α is set to be 0.95 to satisfy the stability for the lengths of stencils used according to Zhong and Tatineni [38]. Figure 2b is a comparison between the uniform and non uniform grid errors. From Fig.2b, the L_∞ error for the non-uniform grid reaches 10^{-14} for the stencil length of 17 in contrast to the error stagnating at 10^{-10} for the uniform grid, which is a stability issue for the uniform grid due to the Runge phenomena near the boundary points. The non-uniform stretching allows high-order accuracy and stability to be maintained at the boundary.

B. Bi-orthogonal Eigenfunction System of Compressible Flow over a Flat Plate

In this section, the goal is to confirm that the discrete and continuous eigenfunctions are computed accurately. These eigenpairs are critical in the bi-orthogonal decomposition and necessary tools for obtain the modal effects of perturbations. Hence, a verification of eigenpairs both discrete and continuous modes against previous work is performed to ensure the correctness of the result. Since the compressible flow over a flat plate is studied in depth in Ref. [21],[14], and [18], the verification examines the eigenpairs in the cases of compressible flow over a flat plate. For the compressible flow over a flat plate, the meanflow profile is obtained according to Malik's formulation [14]. The similarity solution is obtained by performing the following transformation from physical space (x, y) to the transformed space (ξ, η),

$$\begin{aligned} \xi &= \int_0^x \rho_e u_e \mu_e \, \mathrm{d}x \\ \eta &= \frac{u_e}{\sqrt{2\xi}} \int_0^y \rho \mathrm{d}y \end{aligned} \tag{60}$$

where ρ_e, u_e and μ_e are the density, velocity and viscosity at the edge of the boundary layer. In (ξ, η) coordinates, the steady governing equations for a flat plate with no pressure gradient can be written as

$$\begin{aligned} (cf'')' + ff'' &= 0 \\ (a_1 g' + a_2 f' f'')' + fg' &= 0 \end{aligned} \tag{61}$$

where

$$a_1 = c/\sigma, \quad a_2 = \frac{(\gamma-1)M^2}{\left(1 + \frac{(\gamma-1)}{2}\right) M^2} \left(1 - \frac{1}{\sigma}\right) c \tag{62}$$

and

$$f' = u/u_e, \quad g = H/H_e, \quad c = \rho\mu/\rho_e\mu_e. \tag{63}$$

Here, H is the enthalpy and M is the edge mach number. The Prandtl number σ is defined as $\frac{\mu c_p}{k}$, where c_p is the specific heat at constant pressure and assume constant for perfect gas. No slip velocity boundary condition is applied at the wall. The meanflow wall temperature boundary conditions can be varied between an adiabatic wall and an isothermal wall by setting g and g' at the wall. The flat plate meanflow profile is solved by a shooting method using the fourth order Runge Kutta and Newton's method since the flat plate meanflow can be easily converged.

1. Discrete Modes

Mentioned above, Balakumar and Malik [18] and Miselis [28] presented the result for a case of compressible flow over a flat plate with a mach number of 4.5. The stagnation temperature is 311 K. Adiabatic wall meanflow is set. The Prandtl number is 0.72 and the Reynolds number is $Re = 1000$. The non-dimensional circular frequency ω is set to 0.2 and the non-dimensional spanwise wavenumber β is set to 0.12. For clarity purpose, the relation between the dimensional and non-dimensional frequencies are listed as following, where $*$ denotes the dimensional variable.

$$\omega = \frac{\omega^* L^*}{u^*_\infty}, \tag{64}$$

$$F = \frac{2\pi f^* \mu^*_\infty}{\rho^*_\infty u^{*2}_\infty} = \frac{\omega^* \mu^*_\infty}{\rho^*_\infty u^{*2}_\infty}, \tag{65}$$

where the local Reynolds number and the reference boundary layer thickness L^* are formulated as

$$R = \frac{\rho^*_\infty u^*_\infty L^*}{\mu^*_\infty}, \tag{66}$$

and

$$L^* = \sqrt{\frac{\mu^*_\infty x^*}{\rho^*_\infty u^*_\infty}}. \tag{67}$$

The wall pressure is chosen as the normalization variable. The table below is the comparison of results for the case. The finite difference scheme is set to have a stencil length of 11 with the number of grid points $N = 204$. For this case, a single domain non-uniform grid is used. The grid stretching parameter, α_{grid} is set to be 0.99. This parameter is chosen to satisfy the stability trend presented in Ref.[38]. To obtain the initial guesses for the local nonlinear iteration, a global eigendecomposition is performed. The general eigenvalue problem is formulated by setting the nonlinear α^2 dependent term to zero in Eq. (43). Figure 1 shows the global eigenvalues with discrete poles and the discretized continuous branches of this case. The local nonlinear iteration is then applied to obtain the exact values of the two discrete modes. Table 1 presents the computed spatial eigenvalues of the discrete modes in comparison to Ref. [18] and [28].

	Balakumar & Malik (1992)	Miselis (2016), Rk4, $N = 3000$	Finite Difference, $N = 204$
Mode S	$0.2181 + i2.969 \times 10^{-4}$	$0.2181 + i2.973 \times 10^{-4}$	$0.21813 + i2.9734 \times 10^{-4}$
Mode F	$0.2124 + i1.288 \times 10^{-2}$	$0.2124 + i1.288 \times 10^{-2}$	$0.21245 + i1.2886 \times 10^{-2}$

Table 1 Spatial eigenvalue result comparison.

With only $N = 204$ grid points, the finite difference results show no discrepancy up to the given precision comparing with results from Ref. [28]. Figure 3a shows the magnitude of the streamwise velocity component, $|u|$, plotted against the reference eigenfunction in Ref.[28]. Moreover, Figs.3b and 3c show the pressure and temperature profiles of the discrete modes.

The eigenfunctions presented are normalized by the wall pressure. Overall behavior and the mode shape of the two discrete modes align well with reference. The expected freestream decaying behavior is shown in all three perturbation variables. Two critical layers are present in the mode profiles. One correspond to the peak in the temperature profile starting at $y/L = 10$ and the other corresponds to the peak in the streamwise velocity profile starting at the wall. The multi-domain grid can be adjusted to focus on resolving features in the two regions. From both the eignvalues and

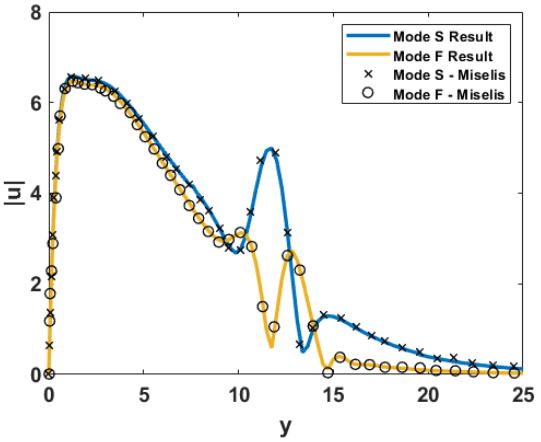

(a) Magnitude of streamwise velocity.

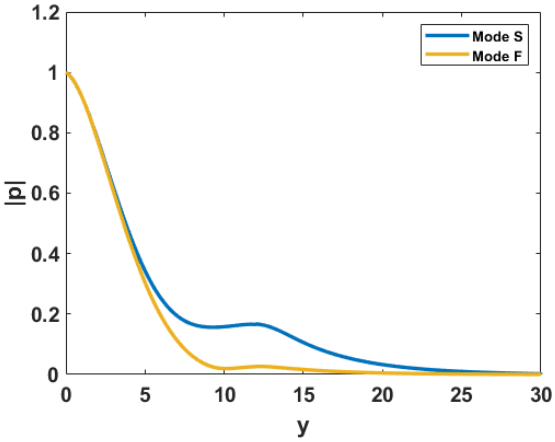

(b) Magnitude of pressure.

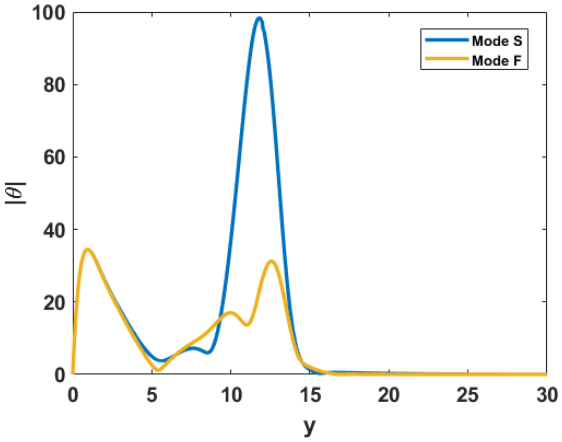

(c) Magnitude of temperature.

Fig. 3 Discrete Mode Results obtained with the direct solve method plotted against Miselis (2016).

eigenfunctions, we can conclude that the finite difference method is correctly implemented with consistency for the flat plate geometry.

2. Continuous Modes

After verifying the discrete mode eigenvalues and eigenfunctions, the next goal is to verify the continuous modes using the finite difference method. Following Tumin [21] and Miselis [28], the verification case is a compressible flow over a flat plate with a mach number of 5.95. The eigenfunctions are normalized by the derivative of streamwise velocity at the wall , $du(0)/dy$ rather than the wall pressure. The value of the branch parameter K is set to 1 in each case. The Prandtl number is set to 0.72 and the bulk viscosity is set to 0.8. Instead of adiabatic wall, the wall temperature to adiabatic wall ratio T_w/T_{ad} is set to 0.1 allowing heat transfer in the meanflow. The non-dimensional frequency F is set to 10^{-4}. The non-dimensional spanwise wave number β is 0.16 and the stagnation temperature is 640 K. The Reynold number is 1500. For the continuous modes, the two boundary conditions, far field extrapolation and asymptotic, are used depending on the different modes for demonstration. In this example, the fast and slow acoustic modes are resolved using the far field extrapolation boundary condition, which only requires one solve of the linear system. Figures 4a and 4b show the streamwise velocity eigenfunctions, plotted against the results given by Tumin [21], for the two continuous acoustic modes. The pressure component is also shown in Fig.4c for analysis of the pressure perturbations in the acoustic modes. Both the real and imaginary components of the eigenfunctions are plotted to showcase the behavior.Here, the non-dimensional wall normal coordinate, y, is normalized by the length of the wall normal profile, L.

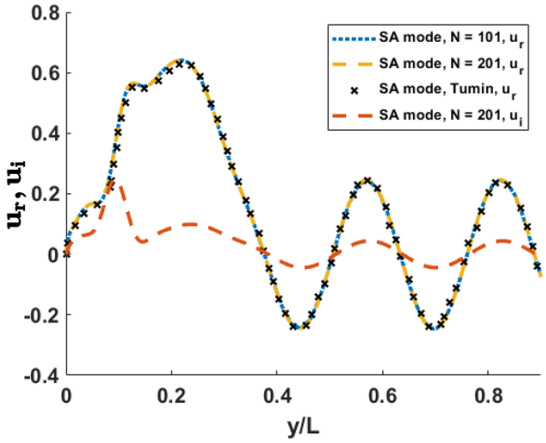

(a) Streamwise velocity for fast acoustic mode.

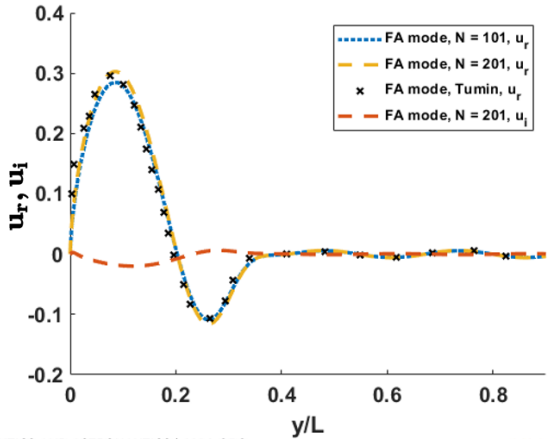

(b) Streamwise velocity for slow acoustic mode.

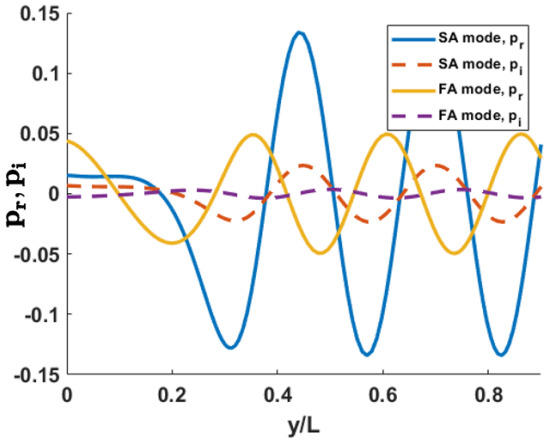

(c) Pressure for slow and fast acoustic modes, $N = 201$**.**

Fig. 4 The computed continuous slow and fast acoustic mode eigenfunctions of streamwise velocity (compared with Tumin (2007)), and pressure.

In Figs. 4a and 4b, a grid convergence test is performed. The results show convergence at as least as $N = 104$. From the streamwise velocity perturbations, the acoustic modes have a larger perturbation amplitude inside the boundary layer and small oscillations continuing into the freestream. This behavior is different in the entropy and vorticity modes, which is presented in the following. For entropy and vorticity modes, we utilized the asymptotic boundary condition. Although the asymptotic boundary condition implementation requires five solves, the advantage is to incorporate the different combinations of the freestream fundamental solutions for modes that contain similar eigenvalues. Fig.5 shows the entropy and vorticity A continuous mode eigenfunctions. The streamwise velocities shown in Figs.5a and 5b are compared with Ref. [21]. The wall-normal velocity and temperature eigenfunctions are also plotted for the vorticity and entropy modes in Figs.5c and 5d. To have a more accurate comparison, the modes in Fig.5 are resolved with $N = 404$ points. The grid stretching parameter, α_{grid} is set to be 0.95 and the length of stencil is also 21.

From the comparison, we can see that the eigenfunctions behave as expected. The small discrepancies in a few area are due to the plot digitization. From the streamwise velocity eigenfunctions, both the entropy and vorticity modes have amplitudes that are higher in the freestream region and do not penetrate into the boundary layer. Moreover, the vorticity mode has a higher wall-normal velocity amplitude in comparison to the entropy mode, which agrees with the physical interpretation of the modes. Likewise, the temperature fluctuation is much higher in the entropy mode. With the above comparisons between the computed results and existing results, the new finite difference method is verified to compute both discrete and continuous modes accurately.

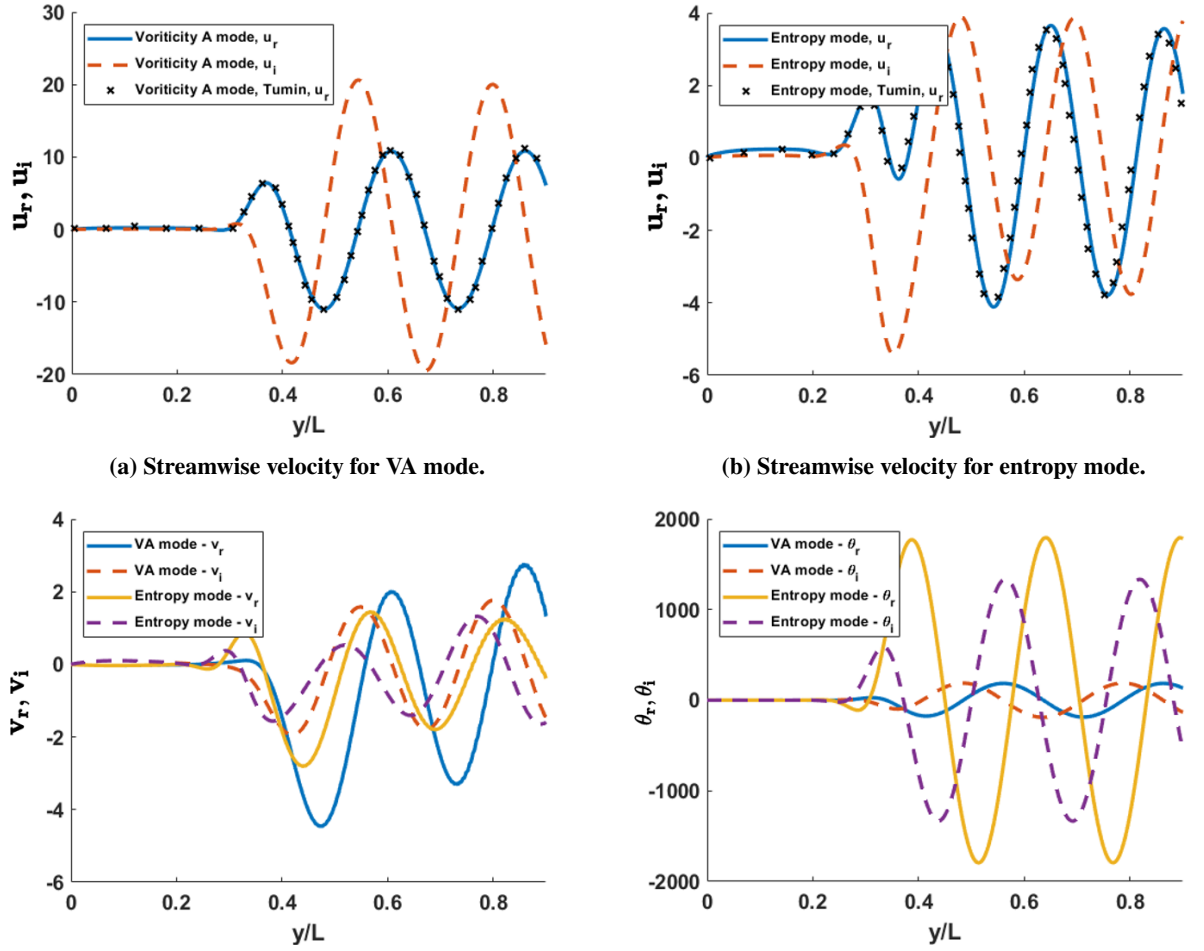

(a) Streamwise velocity for VA mode.

(b) Streamwise velocity for entropy mode.

(c) Wall normal velocity for vorticity A and entropy mode.

(d) Temperature for vorticity A and entropy mode.

Fig. 5 The computed continuous vorticity A and the entropy mode eigenfunctions of streamwise velocity (compared with Tumin (2007)), wall-normal velocity, and temperature.

3. Bi-orthogonal Decomposition

With both the discrete modes and the continuous spectrum verified for different cases, we proceed to the verification of the bi-orthogonal decomposition process. In this process, we use a case with flow conditions the same as the continuous spectrum verification case, but a different Reynold number of 2300. The grid parameters are also the same as the continuous spectrum case. The discrete mode eigenfunctions of this case are shown in Fig.6a and the continuous acoustic modes are shown in Fig.6b.

Since the decomposition purpose is to decompose an arbitrary disturbance and determine the amplitude of influence for each mode. The verification process begins with a composition of direct discrete and continuous modes, carrying different coefficients, to form an arbitrary disturbance.Then we deploy the bi-orthogonal decomposition to decompose the designed disturbance in the attempt to recover the assigned coefficients for each mode. In practice, the inner product of the arbitrary signal and the adjoint modes is performed as the projecting process. For the inner product integration, a composite trapezoidal rule mentioned above is used in the current setting. Figure 7 presents different reconstructed arbitrary signals using the discrete modes and the acoustic modes comparing to Tumin [21].

The design coefficients C used in Fig.7a are $C_S = 1$, $C_F = -1$ and $C_{FA} = 2$. Applying the orthogonality relation, the decomposition of this signal recovers the weights of $C_S = 1.0405 - 4.5385\times10^{-3}i$, $C_F = -9.9667\times10^{-1} + 2.6732\times10^{-2}i$ and $C_{FA} = 1.9999 + 1.2374 \times 10^{-5}i$. The relative error is around 4 percent to the assigned weights. Furthermore, the original coefficients C used in Fig.7b are $C_S = 1$, $C_F = -1$ and $C_{SA} = 2$. The recovered coefficients are $C_S = 1.0186 - 2.7147 \times 10^{-3}i$, $C_F = -1.0155 + 3.8610 \times 10^{-4}i$ and $C_{SA} = 2.0000 - 2.1073 \times 10^{-7}i$ with the largest

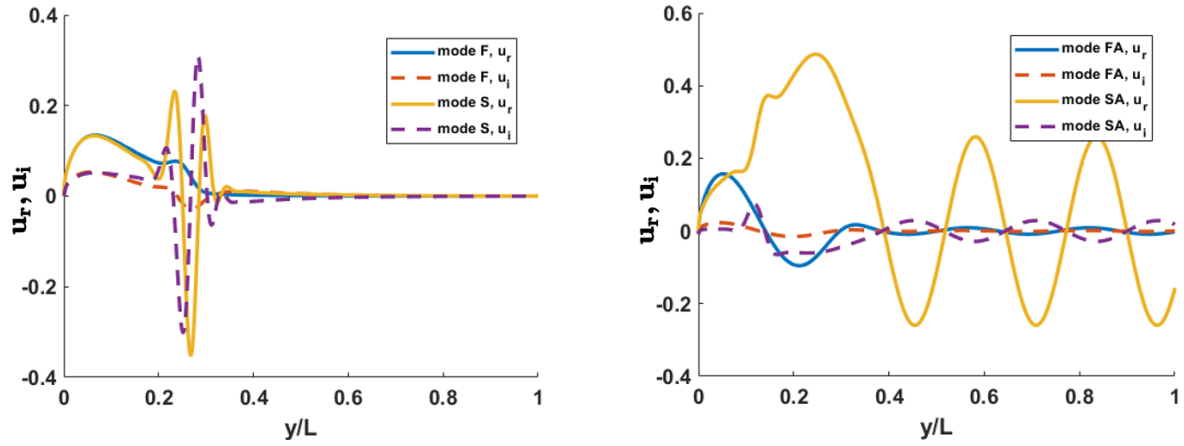

(a) Discrete modes F and S. **(b) Continuous fast and slow acoustic modes.**

Fig. 6 Streamwise velocity component of the discrete and continuous mode used for the bi-orthogonal decomposition verification (flat plate, $K = 1$, $M = 5.95$, $T_w/T_{ad} = 0.1$, $F = 10^{-4}$, $Re = 2300$, $\beta = 0.16$).

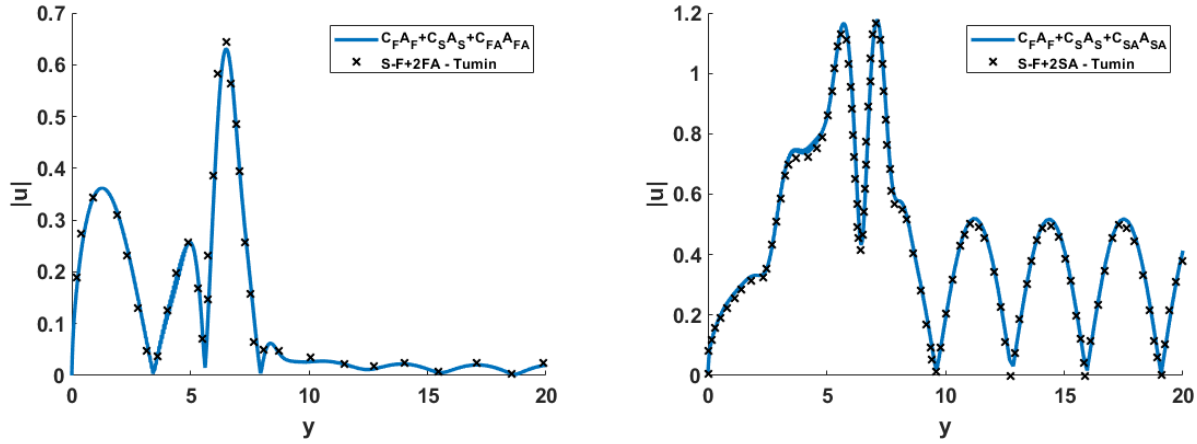

(a) Superposition of mode S, F, and fast acoustic mode. **(b) Superposition of mode S, F, and slow acoustic mode.**

Fig. 7 Reconstructed signal with decomposed coefficients plotted against the original input signal (flat plate, $K = 1$, $M = 5.95$, $T_w/T_{ad} = 0.1$, $F = 10^{-4}$, $Re = 2300$, $\beta = 0.16$).

relative error around 2 percent to the assigned coefficients. From examples above, the very high-order finite difference method to construct the BES has been verified for the case of compressible flow over a flat plate.

C. Bi-orthogonal Eigenfunction System of Hypersonic Flow Over A Blunt Nose Cone

With the verification on the flow over a flat plate, the next step is to develop the BES for the hypersonic flow over a blunt nose cone and analyze the modal effects. For a hypersonic flow over a blunt nose cone, the boundary layer transition is dependent on the initial disturbance amplitude generated by the receptivity of environmental forcing. Current transition prediction procedures, such as the e^N method and the amplitude method by Mack [22], utilize the initial disturbance amplitude (or so called receptivity coefficient) as an important parameter to obtain predictions. The e^N method uses the receptivity coefficient with the aid of the N factor growth rate to obtain the amplified disturbance amplitude at a particular location. Moreover, the amplitude method also relies on the estimated initial and maximum amplitude to iterate for the transition location. Hence, it is critical to obtain an accurate estimation of the initial amplitude or the receptivity coefficient. Currently, the receptivity coefficient is obtained either empirically such as in

Marineau's work [23] or using a combination of LST and DNS result suggested by Yuet and Zhong [24]. Since the experimental procedure of hypersonic flow can be expensive, the computation of receptivity coefficient is crucial. The procedure used by Yuet and Zhong [24] computes the N factor used in the e^N method with an integration of the spatial growth rate, obtained with LST, from the neutrally stable location s_0 to an arbitary location s,

$$N = \int_{s_0}^{s} -\alpha_i \, \mathrm{d}s. \tag{68}$$

Then, the receptivity coefficient or the initial amplitude is a ratio between the Fourier decomposed disturbance amplitude, $A\,(s, f_n)$ obtain from the unsteady DNS data, and the e^N value,

$$C_{\text{rec}}\ (f_n) = A_0\,(f_n) = \frac{A\,(s, f_n)}{e^{N(s,f_n)}}. \tag{69}$$

While this procedure is effective in extracting the second mode receptivity coefficient, which is mostly responsible for breakdown, by sampling the $A\,(s, f_n)$ at a second mode dominant location, the method does not isolate other modes of interest. The amplitude, $A\,(s, f_n)$, from the unsteady DNS result can only be extracted at a location of second mode dominance. Hence, the bi-orthogonal decomposition of the unsteady DNS data is necessary to extract the amplitude of different modes in aids of computing the receptivity coefficient. A receptivity simulation case by He and Zhong [16] [44], refer to Case I, is studied in this context. The steady meanflow of this case is obtained from a high-order shock-fitting direct numerical simulation in a two dimensional axis-symmetric grid. In the DNS code, the conservative Navier Stokes equations are transformed into a computational space with the coordinates (ξ, η, ζ). The physical domain is described by a curvilinear grid that matches the geometry of a blunt nose cone. Figure 8 shows a schematic diagram of the grid over a blunt nose cone.

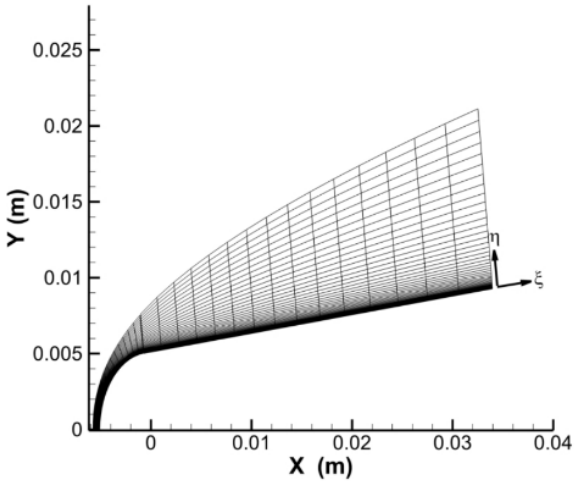

Fig. 8 Schematic diagram of the grid of a blunt cone obtained from He and Zhong [16].

From He and Zhong, the shock is treated as a moving boundary and the flow condition behind the shock is determined with the Rankine-Hugoniot relations. The numerical scheme used is a fifth order upwind scheme for the inviscid fluxes and a sixth order central scheme for the viscous fluxes. Additional details of the general numerical method used for the DNS simulation and the shock-fitting scheme can be found in Zhong [37]. For steady meanflow used in Case I, the blunt nose cone radius is 5.08 mm . The mach number is 9.81. The pressure and density of the freestream are 0.64 kPa and 0.0422 kg/m^3 before the shock. A heat transfer meanflow wall boundary condition is set such that the ratio $T_w/T_0 = 0.3$. The meanflow profiles of a selection of streamwise positions are presented in [16]. Since the mode shape of the velocity and temperature indicates small variations, a quasi parallel assumption is applied such that the meanflow variables are functions of the wall normal direction coordinate only. Under this assumption, the flow field data is divided into wall normal snapshots for each streamwise location and each snapshot at these streamwise sampling locations is analyzed.

1. Discrete Modes

To verify the accuracy of the result, the discrete mode phase speed and the growth rate over a range of streamwise locations are obtained using the high-order finite difference methods and compared with the results from He and Zhong [16], [44]. The local spatial eigenvalues results of each location from spatial analysis are used to derive the local phase speed of a disturbance. The non-dimensional local phase speed of a disturbance for a two dimensional flow is defined as the follow

$$c_r = \frac{(\omega)}{\alpha_r} \tag{70}$$

Following He and Zhong [44], the phase speed and growth rate for a 200 khz disturbance is plotted. This disturbance was chosen due to the significant modal amplification suggested by He and Zhong from the Fourier decomposition of the DNS flow field. Using the multidomain formulation mentioned above, the grid is divided into three zones. The first zone starts from the wall and ends near the peak of the temperature profile, $y_i = 0.08$. The second zone ends where the streamwise velocity component is at 95 percent of the freestream value, $y_o = 0.2$. Half of the grid points are distributed in the first zone and one fourth of the grid points are distributed to each of the following two zones. For the spatial marching, a 10_{th} order finite difference scheme is used with the number of grid points $N = 204$. This results in a sparse linear operator in comparison to the spectral collocation method and significantly lowers the computational time when a large number of locations is analyzed.

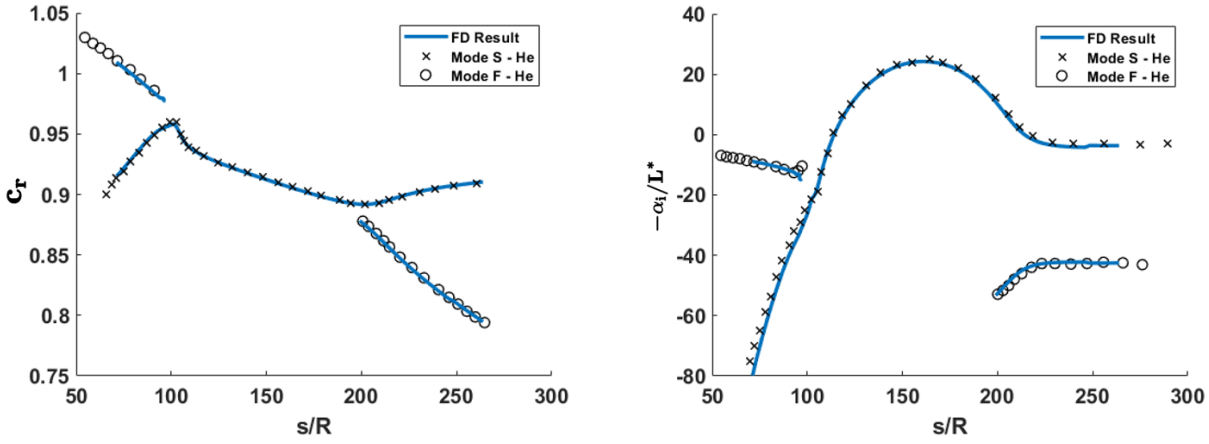

(a) Phase speed of discrete modes F ans S. **(b) Normalize growth rate of discrete modes F and S.**

Fig. 9 Discrete mode F and S phase speed and growth rate obtained from the finite difference method compared against He and Zhong [44].

With a slight mismatch of the upstream mode S growth rate, the result of the finite difference method confirms with previous spectral collocated LST results obtained by He and Zhong. The discrepancy for the upstream mode S growth rate is due to the grid sensitivity of the numerical solution. Yet, overall experiments showed trends closely matching with the reference. The both discrete modes trace back to the originating continuous fast and slow acoustic branches with the phase speeds of $1 + 1/M$ and $1 - 1/M$ going upstream. Furthermore, the finite difference result confirms that the synchronization between discrete mode F and S near the location of $S/R = 100$ and matches the unstable region of the second mode region as expected. Another note is that near the synchronization region, the weaker discrete mode in general will be difficult to resolve numerically due to the similarity in the wavenumber [19], [45]. After the verification of the eigenvalues, the eigenfunctions can also be examined. Figure 10a shows the pressure eigenfunction comparison of against the Case I results obtained with LST using spectral collocation method at the streamwise location of $s* = 1.25\ m$ and a frequency of 260 khz. Figures 10b and 10c are the streamwise velocity and temperature profiles for the discrete modes F and S of the same case. L denotes the length from the wall to the shock here.

From the comparison, the pressure eigenfunction results for both discrete modes F and S align well with the reference. The oscillation of the mode F eigenfunction near the temperature critical region $y/L \approx 0.06$ from the reference is smoothed out in the finite difference result. Numerical experiments also showed that the oscillation in the reference is an effect of the sensitivity to the grid distribution as different grid distributions can produce different oscillation

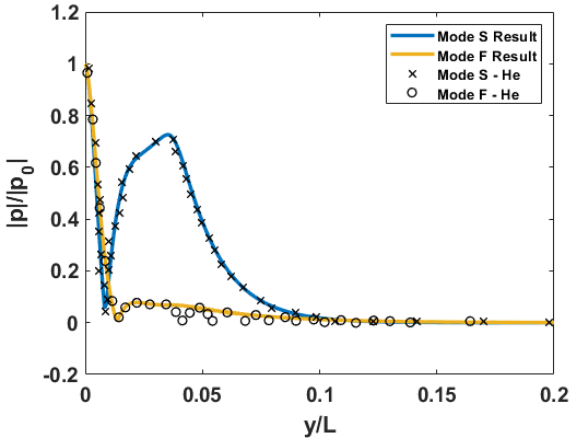

(a) Direct mode S and F pressure eigenfunctions.

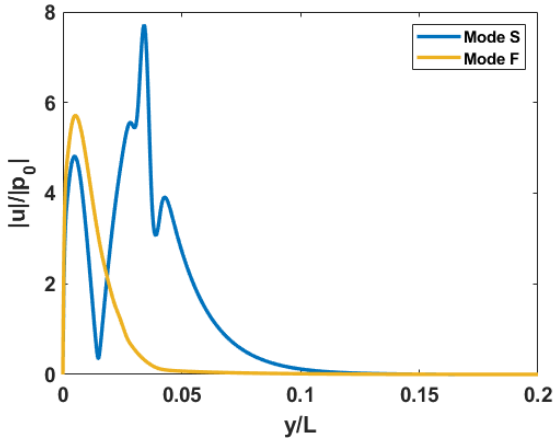

(b) Streamwise velocity.

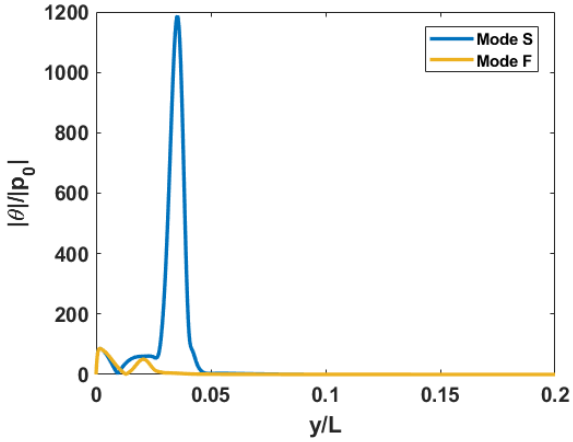

(c) Temperature.

Fig. 10 Discrete mode F and S pressure (comparison against He and Zhong [16]), streamwise velocity and temperature eigenfunctions.

amplitudes in the region. This sensitivity can be due to slight non-parallel effects since this behavior is not recorded for the flat plate cases. Looking at the streamwise velocity and temperature components, we can also identify two critical layers. The location of the temperature critical layer in the discrete mode S aligns with the mean flow profiles shown in Ref,[44]. In this case, a well distributed grid is necessary to well-resolve the critical layers since the solution is more sensitive to the grid. Moreover, the second mode dominance is clearly shown in the higher amplitudes of perturbation variable eigenfunctions.

2. Continuous Modes

After the verification of the discrete mode, the continuous spectrum should be investigated. The finite difference scheme used to obtain the continuous modes has a stencil length of 11 with 404 grid points. The snapshot at the streamwise location of $s* = 1.25\ m$ and a frequency of 200 khz is used as a sample case. The continuous mode eigenfunction results presented below has the value K is set to 1, showing only one location of the continuous branch. From previous studies in Ref. [21], [28], and [18], the vorticity and entropy modes have been concluded to have small contribution to the boundary layer flow. This is due to the rapid decay of the modes after the shock and not penetrating the boundary layer [21]. Figure 11 shows the behavior of the vorticity and entropy mode.

The results indicate that, at the end of the boundary layer, $y/L = 0.2$, both the vorticity and entropy mode decay rapidly and the large freestream oscillations do not penetrate the boundary layer edge as mentioned above. On the other hand,

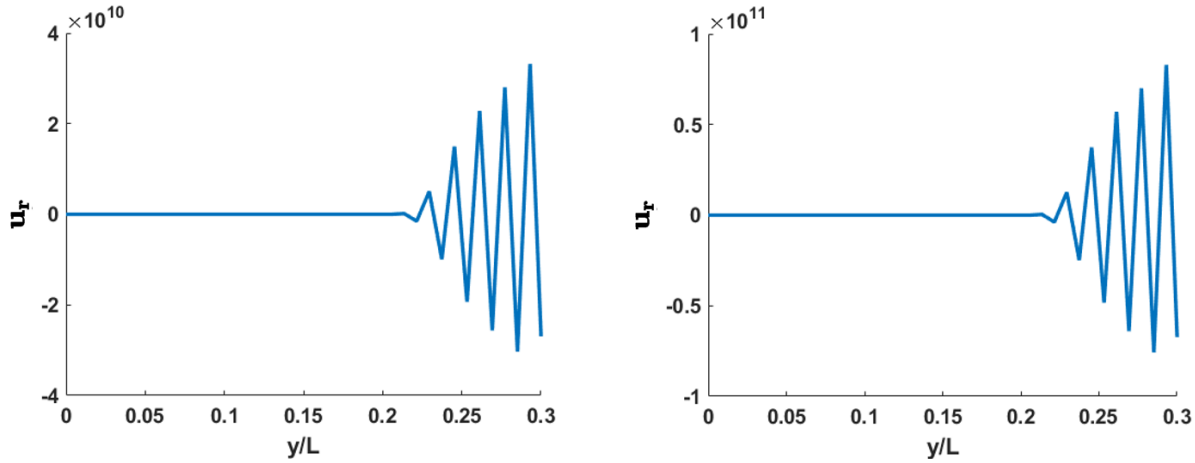

(a) Vorticity A mode eigenfunction. **(b) Entropy mode eigenfunction.**

Fig. 11 Vorticity A and entropy mode results obtained with finite difference method.

the fast and slow acoustic modes have significant perturbations inside the boundary layer comparing to the freestream. Figures 12 and 13 shows the fast and slow acoustic mode velocities and are compared with results obtained with the integration method used by Tumin [21] and Miselis [28]. The integration results are resolved with 3000 grid points and the Gram-Schmidt orthonormalization was performed at each step. The pressure eigenfunctions are also plotted in Fig.12b for fast acoustic and Fig.13b for slow acoustic modes.

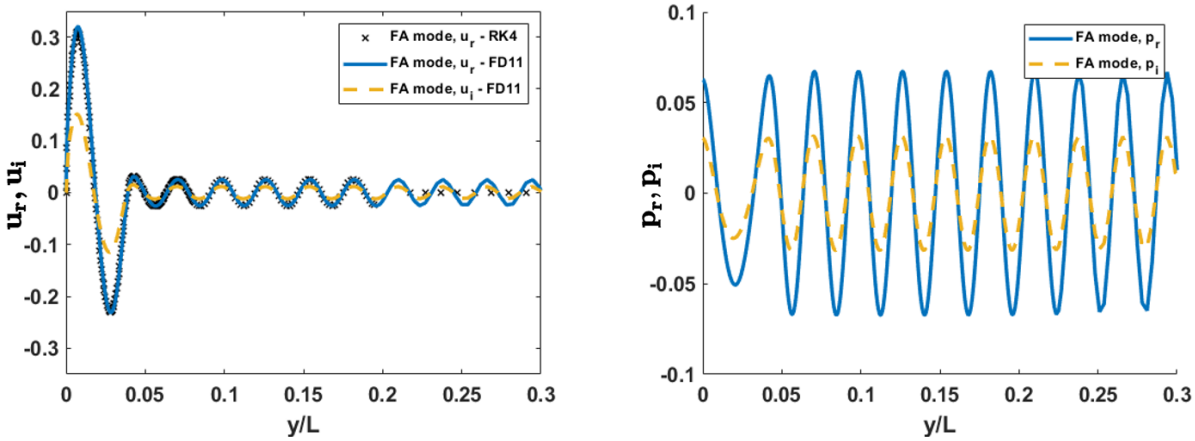

(a) Fast acoustic mode streamwise velocity eigenfunction. **(b) Fast acoustic mode pressure eigenfunction.**

Fig. 12 Fast acoustic mode results obtained with finite difference compared with results obtained from Tumin's integration based shooting method.

The overall result demonstrates agreement to both the behavior described above and to the integration result. Another note is near the end of the boundary layer, the integration method generates numerous singular results especially for the fast acoustic mode. The finite difference method, however, is able to resolve that edge of the boundary layer. The oscillation of the fast acoustic mode also agrees with the behavior of a freestream non-decaying continuous mode. Furthermore, the continuous acoustic functions are observed to have different behavior when a different location of the branch is examined (different values of K). For example, Fig.13 shows the eigenfunction with a discrete K value of 1. From the eigenfunction, a rapid oscillation is observed inside the boundary layer but decaying outside of the boundary layer. However, when the K value is lowered to 0.5, which is closer to the branch point, the continuous eigenfunction oscillation continues onto the freestream. Figure 14 shows the streamwise velocity eigenfunction of the slow acoutic

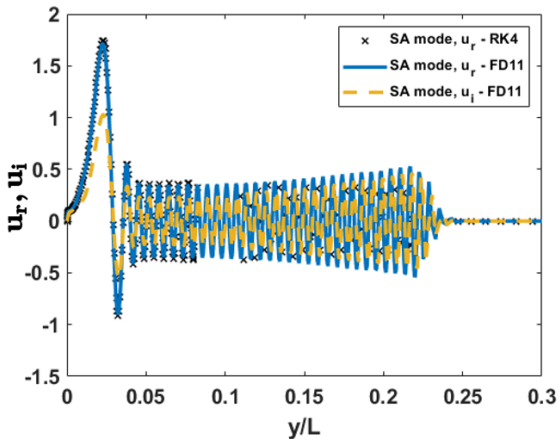

(a) Slow acoustic mode streamwise velocity eigenfunction.

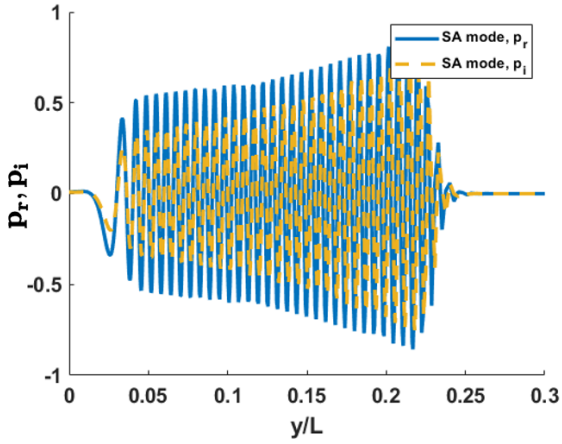

(b) Slow acoustic mode pressure eigenfunction.

Fig. 13 Slow acoustic mode results obtained with finite difference compared with results obtained from Tumin's integration based shooting method.

mode at the branch location of $K = 0.5$.

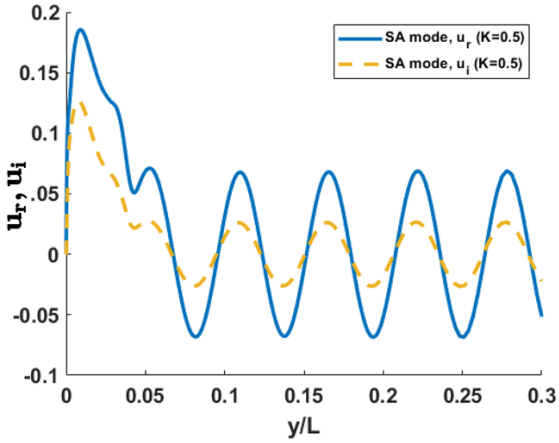

Fig. 14 Slow acoutic eigenfunction result for a K value of 0.5.

3. Bi-orthogonal Decomposition

With the developed discrete and continuous modes, the bi-orthogonal decomposition verification procedure is the same as the flat plate case. An arbitrary disturbance is composed with the direct discrete and continuous modes. The same location and flow conditions are set as the above verification steps. For the continuous mode decomposition, only the fast and slow acoustic modes are considered since the vorticity and entropy modes do not penetrate into the boundary layer. In this orthogonality relationship verification, each continuous branch is discretized with a $\Delta K = 0.25$ for a range values of $K = 0$ to 2. Since the continuous mode is discretized, only one location in the same continuous branch is used in the design of the arbitrary signal to eliminate the non-orthogonality effect of the same branch. Figure 15 shows the streamwise velocity result of an arbitrary signal made up of a combination of mode S, F, and fast acoustic mode with $C_S = 1$, $C_F = -1$, $C_{FA,K=0.5} = -2$. Another case of an arbitrary signal made up of a combination of mode S, F, and slow acoustic mode with $C_S = 1$, $C_F = -1$, $C_{SA,K=0.5} = -2$ is shown in Fig. 16

The blue lines show the reconstructed streamwise velocity and temperature components combined with the different discrete/continuous modes and coefficients resulting from the bi-orthogonal decomposition. The black markers

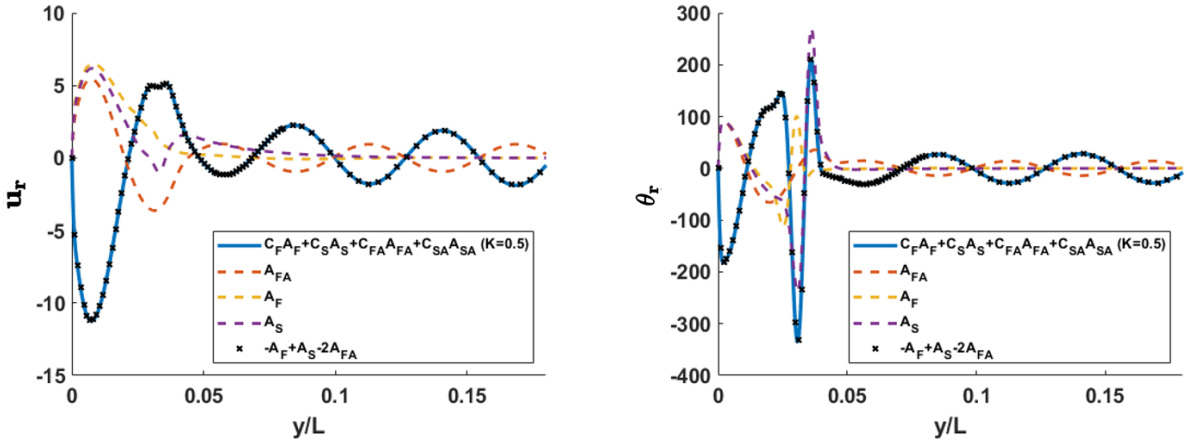

(a) Streamwise velocity. **(b) Temperature.**

Fig. 15 Bi-orthogonal decomposition verification of the blunt nose cone case with discrete modes and fast acoustic continuous mode.

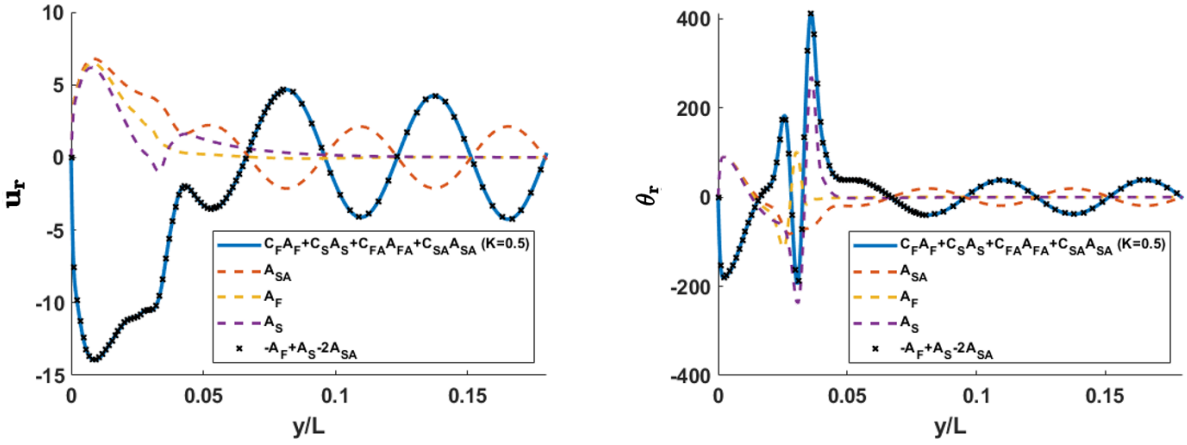

(a) Streamwise velocity. **(b) Temperature.**

Fig. 16 Bi-orthogonal decomposition verification of the blunt nose cone case with discrete modes and slow acoustic continuous mode.

indicate the arbitrary designed perturbation. The bi-orthogonal decomposition of the arbitrary perturbationl shown in Fig. 15 results in coefficients of $C_S = 9.9976 \times 10^{-1} - 5.6270 \times 10^{-3}i$, $C_F = -1.0009 - 3.6908 \times 10^{-2}i$, and $C_{FA,K=0.5} = -1.9998 - 8.1469 \times 10^{-5}i$. The largest relative error to the original coefficient is around 3.7 percent. Moreover, the coefficients of the discetized slow acoustic branch have a maximum magnitude in the order of 10^{-3}. The second decomposition example in Fig. 16 has similar results as well. The resulting coefficients are $C_S = 9.99986 \times 10^{-1} - 5.1401 \times 10^{-4}i$, $C_F = -1.0008 + 1.1651 \times 10^{-3}i$, and $C_{FA,K=0.5} = -2.000 + 2.8032 \times 10^{-6}i$. The coefficients for other branch have the magnitude of 10^{-3} as well.

After the verification of bi-orthogonality between discrete and continuous modes, the unsteady flow field data with a finite spherical slow acoustic disturbance is decomposed to obtain the coefficients of modal influence for each mode. The freestream pulse is modeled as a Gaussian pulse [16] and incorporated into the unsteady DNS simulation,

$$q(x, y, z, t) = |q'|_\infty \exp\left(-\frac{(R_c)^2}{2\sigma^2}\right) + q_\infty. \tag{71}$$

The term q is the disturbance variable and $|q'|_\infty$ stands for the peak freestream perturbation. The term R_c refers to

the radial distance from the center of the pulse to a point in the flow field. The variable σ controls both the spatial width of the pulse as well as the frequency bandwidth of the disturbance. The finite spherical pulse parameters and schematic setup for Case I are provided in [16] and [44]. The slow acoustic disturbance in the freestream has a peak density perturbation amplitude, $|\rho'|_\infty$, of 1×10^{-6} as well as a peak pressure perturbation amplitude $|P'|_\infty = |\rho'|_\infty \gamma$. The parameter σ for the finite spherical pulse is set to 1×10^{-3}. The pulse is set to start the advection at a location $x_0 = -0.02\ m$ with a slow acoustic disturbance speed of $C_\infty = U_\infty - a_\infty$. Since the boardband disturbances are modelled using the Gaussian pulse representation, the unsteady DNS flow field is analyzed with Fourier Transform to obtain the disturbance information in the discrete frequency spectrum. The Fast Fourier Transform (FFT),

$$h\left(t_k\right) \equiv h_k \approx \sum_{n=0}^{N-1} H\left(f_n\right) e^{-2\pi i f_n t_k}, \tag{72}$$

is used to transform all the time dependent perturbation variables, u, p, v, ρ. The perturbation variables are inputted as $h(t_k)$ and outputted as the complex coefficient $H(f_n)$ for the n_{th} frequency in a total of N discrete frequencies. The complex coefficient $H(f_n)$ is then used as the disturbance input, z_{DNS}, to the bi-orthogonal decomposition system for the n_{th} frequency. With the FFT perturbation data at a specific frequency, a projection onto the discrete and continuous modes can be performed. The Case I disturbance flow field at a streamwise location $s* = 1.25\ m$ with a frequency of $200\ khz$ is projected to the discrete and continuous modes in Fig.17. At this streamwise location, a band of frequencies from 160 to 200 khz exhibits high amplification in the surface pressure indicating a second mode response on the neutral curve [44]. Hence, the discrete modes F and S are also plotted for comparison.

From Fig.17, the FFT data aligns closely with both the discrete mode S and the projection result as expected. Moreover, from both the streamwise velocity and the pressure perturbation, the modeshape of the discrete mode S matches better in the region below $y/L = 0.03$ whereas the projection result, especially for pressure, aligns better with the FFT result in the upper area. This region presents the most dominant part of the discrete mode S and other modal/non-modal effects become present after. The coefficients of the two continuous modes for a range of K values from 0 to 4 are also plotted in Fig.18. For each continuous branch, the K value is discretized with a ΔK of 0.05.

Both the slow acoustic and fast acoustic continuous branches have the largest coefficients in the K value range from 0 to 1 which follows the overall trend of the influence of continuous branches presented by [19] [28]. Furthermore, the oscillation in the streamwise velocity component near $y/L = 0.3$ to 0.4, however, is not an effect of the oscillating continuous modes. This might be a contribution to non-modal/transient effects of the modal superposition as the discrete mode S is near the slow acoustic branch at this streamwise location. For further investigations in non-modal effects, input-output analysis mentioned above can also be used in parallel to verify the result. In addition, the computatedl result of an input-output analysis for a hypersonic boundary layer by Nichols and Candler also captures similar non-modal oscillations in mode amplitude which is contributed to energy exchange between modes [34]. The FFT data is also projected onto the vorticity and entropy modes for verification. The coefficients of both modes have a magnitude of 10^{-7} which confirms with the previous studies that these modes do not penetrate into the boundary layer [21] [28]. Knowing the contribution of each mode, various stability analysis methods, such as receptivity coefficients calculation and Mack's amplitude method [22], can be applied in extension.

V. Conclusions

A new general very high-order (10 or higher to spectral-like) finite difference scheme on a non-uniform grid for linear stability theory and bi-orthogonal decomposition is presented in this paper. This new method offers an uniform method to compute both discrete and continuous mode eigenfunctions, which can easily be incorporated into Tumin's bi-orthogonal decomposition framework [21]. Using the boundary value problem approach, the method implementation is straightforward and the need for the complicated Gram-Schimdt orthonormalization and recovery process in the shooting method is avoided. Depending on if the eigenvalue of a specific mode is distinct or not, different boundary conditions for the finite difference method are formulated to compute both discrete and continuous modes. The far field extrapolation boundary condition is computationally efficient and able to compute eigenfunctions with distinct eigenvalues, which correspond to the discrete modes and continuous acoustic modes. The asymptotic boundary condition by the means of freestream fundamental solution is utilized to obtain the eigenfunctions with similar eigenvalues, which correspond to the continuous vorticity and entropy modes. The global eigenvalue decomposition as well as the local spatial eigenvalue search can be performed with minimal modification to the finite difference discrete operators. These discrete operators can also be tuned to have sparse structure or spectral-like resolution as the length of the finite difference

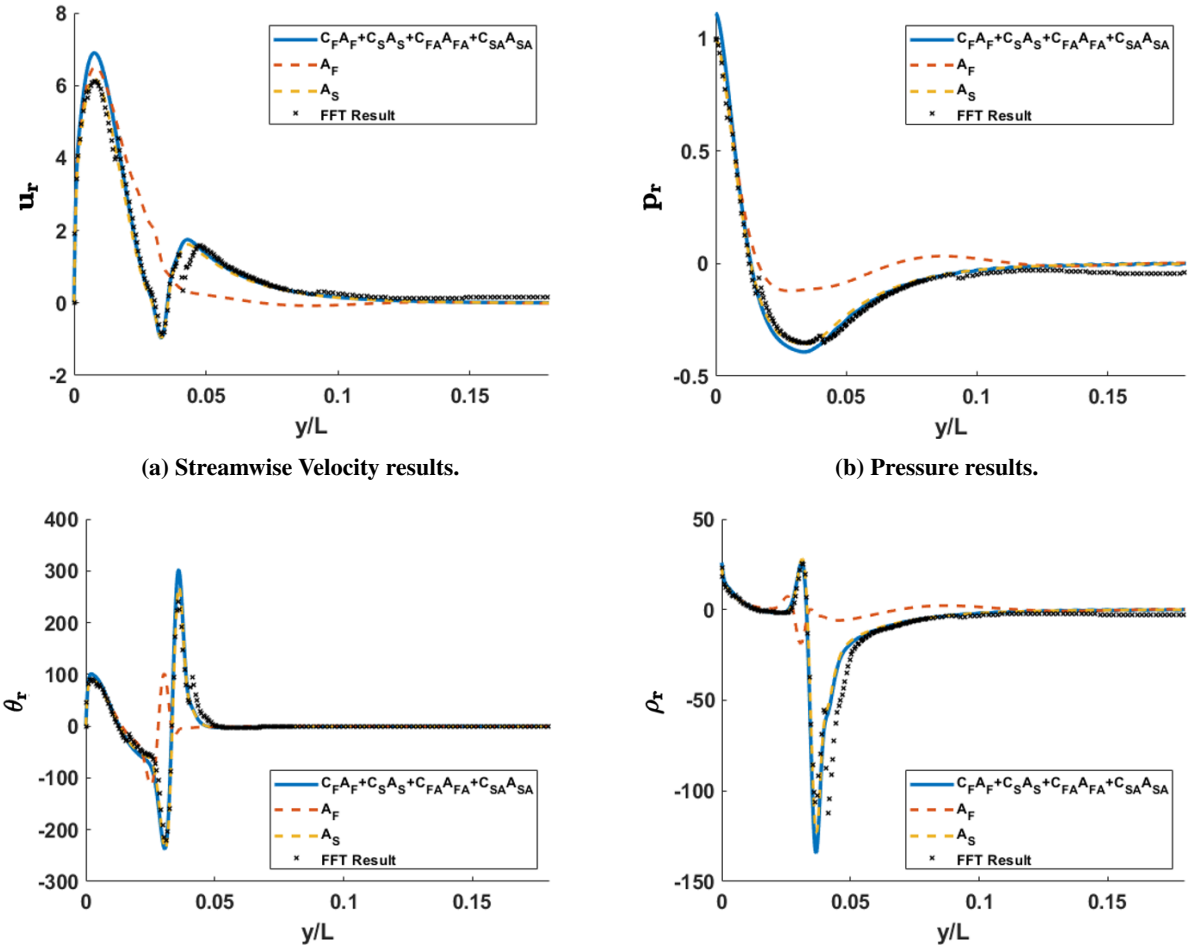

(a) Streamwise Velocity results.

(b) Pressure results.

(c) Temperature results.

(d) Density results.

Fig. 17 Real component of the streamwise velocity component, pressure, temperature, and density projection results obtained with finite difference compared with the original FFT data.

stencil varies. Moreover, the finite difference method utilizes a non-uniform grid distribution with multi-domains to bypass the grid transformation procedure needed for the collocation methods using direct discretization and resolve features in critical layers.

The new numerical method has been applied successfully in two flow scenarios including a supersonic flow over a flat plate and a hypersonic flow over a blunt nose cone. Both the discrete and continuous modes computed by the new method have been verified by comparing with existing studies of supersonic flow over a flat plate and hypersonic flow over a blunt nose cone. It has been found that the results for both discrete and continuous modes for the flat plate case agreed well to previous results from the work of Tumin[21], Miselis[28], and Balakumar[18]. Subsequently, the bi-orthogonal decomposition for the supersonic flow over a flat plate has also been performed on a designed disturbance with known coefficients. The recovered amplitude coefficients for each mode using the bi-orthogonal decomposition also matches closely with the assigned coefficients, which confirms the orthogonality between the resulting modes.

The new method was then applied to aid the receptivity study of a hypersonic flow over a blunt nose cone. The bi-orthogonal eigenfunction system (BES) of discrete and continuous modes has been computed by the new method for the hypersonic flow over a blunt nose cone using the steady DNS meanflow data provide by He and Zhong [16]. Both the computed discrete mode phase speed and growth rate aligned well with previous results in He's work. The eigenfunctions of the discrete modes also compared well with critical layers well resolved. Furthermore, the continuous modes obtained with the new method also displayed behaviors agreeing with the physics. With these discrete and continuous modes obtained for the hypersonic flow over a blunt cone, the bi-orthogonal decomposition of the unsteady

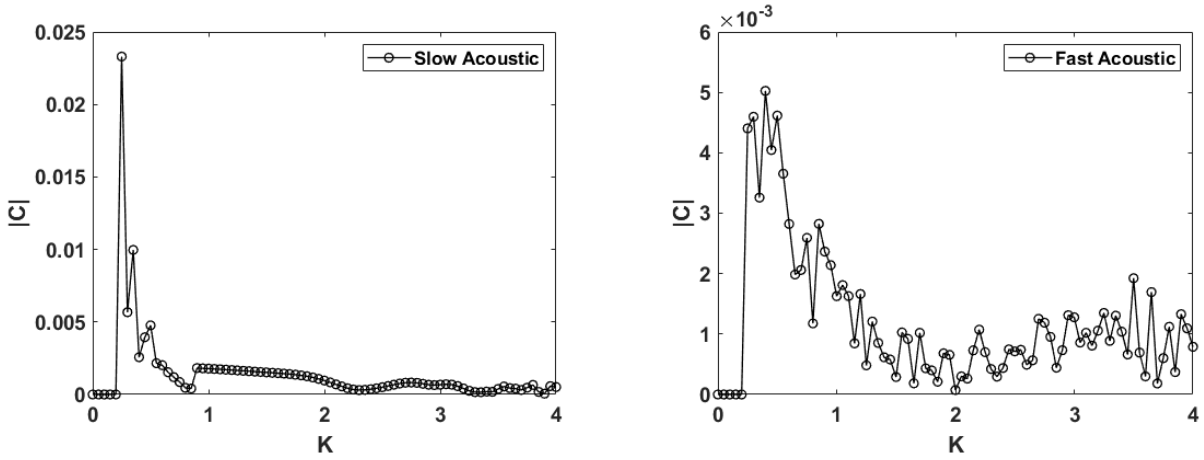

(a) Slow acoustic mode coefficients. **(b) Fast acoustic mode coefficients.**

Fig. 18 The magnitude of projected coefficients of the slow acoustic and fast acoustic .

DNS flow field of a receptivity simulation has been performed.

The bi-orthogonal decomposition is particularly useful in the freestream receptivity study of hypersonic flow over a blunt body for a better understanding of the dominant source of the disturbance. Various transition prediction tools such as e^N method and the amplitude method by Mack [22] relies on an accurate initial disturbance amplitude, or so called receptivity coefficient, to predict the transition location. Yet, the initial perturbation at the branch I neutral stability point, where the instability starts on the neutral curve, is composed of weak perturbations from different modes. Current computational approach for obtaining the receptivity coefficient is an approximated approach that backtracks the initial amplitude using the growth rate of the unstable mode and the disturbance amplitude obtained by DNS at a location where the unstable mode is dominant [16]. However, using discrete and continuous modes computed by the new method, the modal decomposition of the initial perturbation can be applied easily to obtain the modal receptivity coefficients. Hence, a bi-orthogonal decomposition of the unsteady DNS flow field data from a freestream receptivity simulation by He and Zhong [16] also has been performed with preliminary results shown. This is done by applying the orthogonality relation to the Fourier transformed flow field data at a specific frequency and projecting the perturbation variables onto the bi-orthogonal eigenfunctions to obtain the modal perturbation amplitudes. The result of the decomposition aligned with the existing observation of the discrete mode S being dominant in the second mode instability region.

As the focus of this paper is on the numerical results, next step of this research will be the application of the new method to study the flow physics of hypersonic flow receptivity over a blunt nose cone. Immediate application of the new method will be the computation of the receptivity coefficients for each mode in the upstream location, which is needed for transition predicting tools such as the e^N method and the amplitude method by Mack [22]. Moreover, since various freestream disturbances such as acoustic/entropy/vorticity and finite/planar disturbances causes different perturbation behaviors, the corresponding flow fields can also be decomposed to investigate the modal contributions [16]. Further considerations of the non-parallel effects in the blunt nose cone geometry can be added using the method of multiple scales [46] and the parabolized stability equations [47]. Furthermore, the discrete operator formulated in this paper can be applied as the linear operator for the input-output analysis if needed. In addition, with this tool of general very high-order accuracy, extensions to different flow conditions such as the real gas flow can be performed to build a more physical model and better reveal the characteristics in the study of hypersonic boundary layer transition.

A. The Matrix Elements

The matrix elements of $\mathbf{H}_0$ in Eq. (17) are presented here. Similar to Ref. [28], [21], we define $r = 2(\epsilon + 2)/3$ and $m = 2(\epsilon - 1)/3$ where ϵ is the ratio of bulk viscosity to dynamic viscosity and equals to 0 following Stoke's hypothesis. For entries not specified, the coefficients equal to zero. We first define,

$$\chi = \left[\frac{Re}{\mu} - \frac{i\hat{\omega}r}{P}\right]^{-1} \tag{73}$$
$$\hat{\omega} = \omega - \alpha U.$$

For $\mathbf{H}_0$, we have

$$H_0^{1,2} = 1$$
$$H_0^{2,1} = \alpha^2 + \beta^2 - i\hat{\omega}P\gamma M^2\frac{Re}{\mu T}$$
$$H_0^{2,2} = -\frac{1}{\mu}\frac{\partial \mu}{\partial y}$$
$$H_0^{2,3} = -i\alpha(m+1)\frac{1}{T}\frac{\partial T}{\partial y} - i\alpha\frac{1}{\mu}\frac{\partial \mu}{\partial y} + \mathrm{Re}\,P\gamma M^2\frac{1}{\mu T}\frac{\partial U}{\partial y} + i\alpha(m+1)\frac{1}{P}\frac{\partial P}{\partial y}$$
$$H_0^{2,4} = i\alpha\frac{Re}{\mu} + \alpha\hat{\omega}(m+1)\frac{1}{P}$$
$$H_0^{2,5} = -\alpha\hat{\omega}(m+1)\frac{1}{T} - \frac{1}{\mu}\left(\frac{\partial T}{\partial y}\frac{\partial U}{\partial y}\frac{\partial^2 \mu}{\partial T^2} + \frac{\partial \mu}{\partial T}\frac{\partial^2 U}{\partial y^2}\right)$$
$$H_0^{2,6} = -\frac{1}{\mu}\frac{\partial \mu}{\partial T}\frac{\partial U}{\partial y}$$
$$H_0^{3,1} = -i\alpha$$
$$H_0^{3,3} = \frac{1}{T}\frac{\partial T}{\partial y} - \frac{1}{P}\frac{\partial P}{\partial y}$$
$$H_0^{3,4} = \frac{i\hat{\omega}}{P}$$
$$H_0^{3,5} = -\frac{i\hat{\omega}}{T}$$
$$H_0^{3,7} = -i\beta$$
$$H_0^{4,1} = -i\chi\alpha\left(r\frac{1}{T}\frac{\partial T}{\partial y} + \frac{2}{\mu}\frac{\partial \mu}{\partial y} - r\frac{1}{P}\frac{\partial P}{\partial y}\right)$$
$$H_0^{4,2} = -i\chi\alpha$$
$$H_0^{4,3} = \chi\left(-\alpha^2 - \beta^2 + i\hat{\omega}P\gamma M^2\frac{Re}{\mu T} + r\frac{1}{T}\frac{\partial^2 T}{\partial y^2} + r\frac{1}{\mu T}\frac{\partial \mu}{\partial y}\frac{\partial T}{\partial y} - r\frac{1}{\mu P}\frac{\partial \mu}{\partial y}\frac{\partial P}{\partial y} + 2r\frac{1}{P^2}\left[\frac{\partial P}{\partial y}\right]^2 - 2r\frac{1}{PT}\frac{\partial P}{\partial y}\frac{\partial T}{\partial y}\right.$$
$$\left. -r\frac{1}{P}\frac{\partial^2 P}{\partial y^2}\right)$$
$$H_0^{4,4} = -i\chi r\frac{1}{P}\left(\alpha\frac{\partial U}{\partial y} - \hat{\omega}\frac{1}{T}\frac{\partial T}{\partial y} - \hat{\omega}\frac{1}{\mu}\frac{\partial \mu}{\partial y} + 2\hat{\omega}\frac{1}{PT}\frac{\partial P}{\partial y}\right)$$
$$H_0^{4,5} = i\chi\left(\alpha r\frac{1}{T}\frac{\partial U}{\partial y} + \alpha\frac{1}{\mu}\frac{\partial \mu}{\partial T}\frac{\partial U}{\partial y} - r\hat{\omega}\frac{1}{\mu T}\frac{\partial \mu}{\partial y} + r\hat{\omega}\frac{1}{PT}\frac{\partial P}{\partial y}\right)$$
$$H_0^{4,6} = -i\chi r\hat{\omega}\frac{1}{T}$$
$$H_0^{4,7} = -i\chi\beta\left(r\frac{1}{T}\frac{\partial T}{\partial y} + 2\frac{1}{\mu}\frac{\partial \mu}{\partial y} - r\frac{1}{P}\frac{\partial P}{\partial y}\right)$$
$$H_0^{4,8} = -i\chi\beta$$
$$H_0^{5,6} = 1$$
$$H_0^{6,2} = -2(\gamma-1)M^2\,\mathrm{Pr}\frac{\partial U}{\partial y}$$

$$
\begin{aligned}
H_0^{6,3} &= -2i\alpha(\gamma-1)M^2\,\mathrm{Pr}\,\frac{\partial U}{\partial y} + \mathrm{P}\gamma\,M^2\,\mathrm{Pr}\,\frac{\mathrm{Re}}{\mu T}\frac{\partial T}{\partial y} - (\gamma-1)M^2\,\mathrm{Pr}\,\frac{\mathrm{Re}}{\mu}\frac{\partial P}{\partial y}\\
H_0^{6,4} &= i\hat{\omega}(\gamma-1)M^2\,\mathrm{Pr}\,\frac{\mathrm{Re}}{\mu}\\
H_0^{6,5} &= \alpha^2+\beta^2 - i\hat{\omega}\,\mathrm{Pr}\,M^2\,\mathrm{Pr}\,\frac{\mathrm{Re}}{\mu T} - (\gamma-1)M^2\,\mathrm{Pr}\,\frac{1}{\mu}\frac{\partial \mu}{\partial T}\left(\frac{\partial U}{\partial y}\right)^2 - \frac{1}{\mu}\frac{\partial^2\mu}{\partial y^2}\\
H_0^{6,6} &= -\frac{2}{\mu}\frac{\partial \mu}{\partial y}\\
H_0^{7,8} &= 1\\
H_0^{8,3} &= -i\beta(m+1)\frac{1}{T}\frac{\partial T}{\partial y} - i\beta\frac{1}{\mu}\partial\mu\partial y + i\beta(m+1)\frac{1}{P}\frac{\partial P}{\partial y}\\
H_0^{8,4} &= \beta\hat{\omega}(m+1)\frac{1}{P} + i\beta\frac{Re}{\mu}\\
H_0^{8,5} &= -\beta\hat{\omega}(m+1)\frac{1}{T}\\
H_0^{8,7} &= \alpha^2+\beta^2 - i\hat{\omega}P\gamma M^2\frac{Re}{\mu T}\\
H_0^{8,8} &= -\frac{1}{\mu}\frac{\partial \mu}{\partial y}
\end{aligned}
$$

B. Asymptotic Result

Before presenting the asymptotic results, the following terms have to be defined,

$$
\begin{aligned}
b_{11} &= H_0^{21}\\
b_{22} &= H_0^{42}H_0^{24} + H_0^{43}H_0^{34} + H_0^{46}H_0^{64} + H_0^{48}H_0^{84}\\
b_{23} &= H_0^{42}H_0^{25} + H_0^{43}H_0^{35} + H_0^{46}H_0^{65} + H_0^{48}H_0^{85}\\
b_{32} &= H_0^{64}, b_{33} = H_0^{65}.
\end{aligned}
\tag{74}
$$

The eigenvalues are

$$
\begin{aligned}
\lambda_{1,2}^2 &= \lambda_{7,8}^2 = b_{11} = \alpha^2+\beta^2+\mathrm{i}\,\mathrm{Re}(\alpha-\omega)\\
\lambda_{3,4}^2 &= (b_{22}+b_{33})/2 + \frac{1}{2}\sqrt{(b_{22}-b_{33})^2+4b_{23}b_{32}}\\
\lambda_{5,6}^2 &= (b_{22}+b_{33})/2 - \frac{1}{2}\sqrt{(b_{22}-b_{33})^2+4b_{23}b_{32}}
\end{aligned}
\tag{75}
$$

with the corresponding eigenvectors

$$
\begin{aligned}
u_{1,2}^0 &= \left(1, \lambda_{1,2}, H_0^{31}/\lambda_{1,2}, 0, 0, 0, 0, 0\right)^T\\
u_{7,8}^0 &= \left(0, 0, H_0^{37}/\lambda_{7,8}, 0, 0, 0, 1, \lambda_{7,8}\right)^T
\end{aligned}
\tag{76}
$$

for the first and last pairs, and

$$
\begin{aligned}
u_{1j}^0 &= 1, \quad u_{2j}^0 = \lambda_j, \quad u_{4j}^0 = \left(\lambda_j^2 - H_0^{21}\right)b_{23}/b_{12}\\
u_{5j}^0 &= -\left(b_{22}-\lambda_j^2\right)\left(\lambda_j^2 - H_0^{21}\right)/b_{12}, \quad u_{6j}^0 = \lambda_j u_{5j}^0\\
u_{7j}^0 &= \left(H_0^{84}u_{4j}^0 + H_0^{85}u_{5j}^0\right)/\left(\lambda_j^2 - H_0^{87}\right), \quad u_{8j}^0 = \lambda_j u_{7j}^0,\\
u_{3j}^0 &= \left(H_0^{31}u_{1j}^0 + H_0^{34}u_{4j}^0 + H_0^{35}u_{5j}^0 + H_0^{37}u_{7j}^0\right)/\lambda_j
\end{aligned}
\tag{77}
$$

for $j = 3, 4, 5, 6$, where $b_{12} = H_0^{24} b_{23} - H_0^{25} \left(b_{22} - \lambda_j^2 \right)$.

Acknowledgments

The first author would like to acknowledge the support by the departmental research fellowship from the UCLA Mechanical and Aerospace Engineering department. Primary computational resources used for the hypersonic meanflow over a blunt cone were provided by Extreme Science and Engineering Discovery Environment (XSEDE) through the Texas Advanced Computing Center (TACC) and San Diego Super- computer Center (SDSC).

References

[1] Zhong, X., and Wang, X., "Direct Numerical Simulation on the Receptivity, Instability, and Transition of Hypersonic Boundary Layers," *Annual Review of Fluid Mechanics*, Vol. 44, No. 1, 2012, pp. 527–561. https://doi.org/10.1146/annurev-fluid-120710-101208, URL https://doi.org/10.1146/annurev-fluid-120710-101208.

[2] V., M., "Transition in open flow systems-a reassessment," *Bull. Am. Phys. Soc.*, Vol. 39, 1994, p. 1882. URL https://cir.nii.ac.jp/crid/1573950400137520256.

[3] Saric, W. S., Reed, H. L., and Kerschen, E. J., "BOUNDARY-LAYER RECEPTIVITY TO FREESTREAM DISTURBANCES," *Annual Review of Fluid Mechanics*, Vol. 34, No. 1, 2002, pp. 291–319. https://doi.org/10.1146/annurev.fluid.34.082701.161921, URL https://doi.org/10.1146/annurev.fluid.34.082701.161921.

[4] MA, Y., and ZHONG, X., "Receptivity of a supersonic boundary layer over a flat plate. Part 1. Wave structures and interactions," *Journal of Fluid Mechanics*, Vol. 488, 2003, p. 31–78. https://doi.org/10.1017/S0022112003004786.

[5] Salwen, H., and Grosch, C. E., "The continuous spectrum of the Orr-Sommerfeld equation. Part 2. Eigenfunction expansions," *Journal of Fluid Mechanics*, Vol. 104, 1981, p. 445–465. https://doi.org/10.1017/S0022112081002991.

[6] Tumin, A., and Fedorov, A., "Spatial growth of disturbances in a compressible boundary layer," *Journal of Applied Mechanics and Technical Physics*, Vol. 24, No. 4, 1983, pp. 548–554. https://doi.org/10.1007/BF00907906.

[7] Mack, L. M., "Boundary-layer linear stability theory," Tech. rep., California Inst of Tech Pasadena Jet Propulsion Lab, 1984.

[8] Fedorov, A., and Tumin, A., "High-Speed Boundary-Layer Instability: Old Terminology and a New Framework," *AIAA Journal*, Vol. 49, No. 8, 2011, pp. 1647–1657. https://doi.org/10.2514/1.J050835, URL https://doi.org/10.2514/1.J050835.

[9] Fedorov, A., "Transition and Stability of High-Speed Boundary Layers," *Annual Review of Fluid Mechanics*, Vol. 43, No. 1, 2011, pp. 79–95. https://doi.org/10.1146/annurev-fluid-122109-160750, URL https://doi.org/10.1146/annurev-fluid-122109-160750.

[10] Mack, L. M., "A numerical study of the temporal eigenvalue spectrum of the Blasius boundary layer," *Journal of Fluid Mechanics*, Vol. 73, No. 3, 1976, p. 497–520. https://doi.org/10.1017/S002211207600147X.

[11] Grosch, C. E., and Salwen, H., "The continuous spectrum of the Orr-Sommerfeld equation. Part 1. The spectrum and the eigenfunctions," *Journal of Fluid Mechanics*, Vol. 87, No. 1, 1978, p. 33–54. https://doi.org/10.1017/S0022112078002918.

[12] Zhigulev, V. N., Sidorenko, N. V., and Tumin, A. M., "The generation of instability waves in a boundary layer having external turbulence," *PMTF Zhurnal Prikladnoi Mekhaniki i Tekhnicheskoi Fiziki*, 1980, pp. 43–49.

[13] Scott, M. R., and Watts, H. A., "Computational solution of linear two-point boundary value problems via orthonormalization," *SIAM Journal on Numerical Analysis*, Vol. 14, No. 1, 1977, pp. 40–70.

[14] Malik, M., "Numerical methods for hypersonic boundary layer stability," *Journal of Computational Physics*, Vol. 86, No. 2, 1990, pp. 376–413. https://doi.org/https://doi.org/10.1016/0021-9991(90)90106-B, URL https://www.sciencedirect.com/science/article/pii/002199919090106B.

[15] Haley, C. L., and Zhong, X., *Mode F/S Wave Packet Interference And Acoustic-like Emissions in a Mach 8 Flow Over a Cone*, AIAA, 2020. https://doi.org/10.2514/6.2020-1579, URL https://arc.aiaa.org/doi/abs/10.2514/6.2020-1579.

[16] He, S., and Zhong, X., "The effects of nose bluntness on broadband disturbance receptivity in hypersonic flow," *Physics of Fluids*, Vol. 34, No. 5, 2022, p. 054104. https://doi.org/10.1063/5.0088236, URL https://doi.org/10.1063/5.0088236.

[17] Varma, A., and Zhong, X., *Hypersonic Boundary-Layer Receptivity to a Freestream Entropy Pulse with Real-Gas and Nose Bluntness Effects*, AIAA, 2020. https://doi.org/10.2514/6.2020-2994, URL https://arc.aiaa.org/doi/abs/10.2514/6.2020-2994.

[18] Balakumar, P., and Malik, M. R., "Discrete modes and continuous spectra in supersonic boundary layers," *Journal of Fluid Mechanics*, Vol. 239, 1992, p. 631–656. https://doi.org/10.1017/S0022112092004555.

[19] Tumin, A., "Multimode decomposition of spatially growing perturbations in a two-dimensional boundary layer," *Physics of Fluids*, Vol. 15, No. 9, 2003, pp. 2525–2540. https://doi.org/10.1063/1.1597453, URL https://doi.org/10.1063/1.1597453.

[20] Gaydos, P., and Tumin, A., "Multimode decomposition in compressible boundary layers," *AIAA journal*, Vol. 42, No. 6, 2004, pp. 1115–1121.

[21] Tumin, A., "Three-dimensional spatial normal modes in compressible boundary layers," *Journal of Fluid Mechanics*, Vol. 586, 2007, pp. 295–322.

[22] Mack, L. M., "Transition and laminar instability," Tech. rep., 1977.

[23] Marineau, E. C., "Prediction Methodology for Second-Mode-Dominated Boundary-Layer Transition in Wind Tunnels," *AIAA Journal*, Vol. 55, No. 2, 2017, pp. 484–499. https://doi.org/10.2514/1.J055061, URL https://doi.org/10.2514/1.J055061.

[24] Huang, Y., and Zhong, X., "Numerical Study of Hypersonic Boundary-Layer Receptivity with Freestream Hotspot Perturbations," *AIAA Journal*, Vol. 52, No. 12, 2014, pp. 2652–2672. https://doi.org/10.2514/1.J052657, URL https://doi.org/10.2514/1.J052657.

[25] Hasnine, S. M. A. A., Russo, V., Browne, O. M., Tumin, A., and Brehm, C., *Disturbance Flow Field Analysis of Particulate Interaction with High Speed Boundary Layers*, AIAA, 2020. https://doi.org/10.2514/6.2020-3046, URL https://arc.aiaa.org/doi/abs/10.2514/6.2020-3046.

[26] Saikia, B., Al Hasnine, S., and Brehm, C., "On the role of discrete and continuous modes in a cooled high-speed boundary layer flow," *Journal of Fluid Mechanics*, Vol. 942, 2022, p. R7. https://doi.org/10.1017/jfm.2022.380.

[27] Tumin, A., Wang, X., and Zhong, X., "Numerical Simulation and Theoretical Analysis of Perturbations in Hypersonic Boundary Layers," *AIAA Journal*, Vol. 49, No. 3, 2011, pp. 463–471. https://doi.org/10.2514/1.J050431, URL https://doi.org/10.2514/1.J050431.

[28] Miselis, M., Huang, Y., and Zhong, X., *Modal Analysis of Receptivity Mechanisms for a Freestream Hot-Spot Perturbation on a Blunt Compression-Cone Boundary Layer*, AIAA, 2016. https://doi.org/10.2514/6.2016-3345, URL https://arc.aiaa.org/doi/abs/10.2514/6.2016-3345.

[29] Tumin, A., "The biorthogonal eigenfunction system of linear stability equations: A survey of applications to receptivity problems and to analysis of experimental and computational results." *41st AIAA Fluid Dynamics Conference and Exhibit*, 2011, p. 3244.

[30] McKEON, B. J., and SHARMA, A. S., "A critical-layer framework for turbulent pipe flow," *Journal of Fluid Mechanics*, Vol. 658, 2010, p. 336–382. https://doi.org/10.1017/S002211201000176X.

[31] JOVANOVIĆ, M. R., and BAMIEH, B., "Componentwise energy amplification in channel flows," *Journal of Fluid Mechanics*, Vol. 534, 2005, p. 145–183. https://doi.org/10.1017/S0022112005004295.

[32] Dwivedi, A., Sidharth, G. S., and Jovanović, M. R., "Oblique transition in hypersonic double-wedge flow," , 2021. https://doi.org/10.48550/ARXIV.2111.15153, URL https://arxiv.org/abs/2111.15153.

[33] Cook, D. A., Thome, J., Brock, J. M., Nichols, J. W., and Candler, G. V., *Understanding effects of nose-cone bluntness on hypersonic boundary layer transition using input-output analysis*, AIAA, 2018. https://doi.org/10.2514/6.2018-0378, URL https://arc.aiaa.org/doi/abs/10.2514/6.2018-0378.

[34] Nichols, J. W., and Candler, G. V., *Input-output analysis of complex hypersonic boundary layers*, AIAA, 2019. https://doi.org/10.2514/6.2019-1383, URL https://arc.aiaa.org/doi/abs/10.2514/6.2019-1383.

[35] Bae, H. J., Dawson, S. T., and McKeon, B. J., *Studying the effect of wall cooling in supersonic boundary layer flow using resolvent analysis*, AIAA, 2020. https://doi.org/10.2514/6.2020-0575, URL https://arc.aiaa.org/doi/abs/10.2514/6.2020-0575.

[36] Chu, B. T., "On the energy transfer to small disturbances in fluid flow (Part I)," *Acta Mechanica*, Vol. 1, 1965, pp. 215–234.

[37] Zhong, X., "High-Order Finite-Difference Schemes for Numerical Simulation of Hypersonic Boundary-Layer Transition," *Journal of Computational Physics*, Vol. 144, No. 2, 1998, pp. 662–709. https://doi.org/https://doi.org/10.1006/jcph.1998.6010, URL https://www.sciencedirect.com/science/article/pii/S0021999198960107.

[38] Zhong, X., and Tatineni, M., "High-order non-uniform grid schemes for numerical simulation of hypersonic boundary-layer stability and transition," *Journal of Computational Physics*, Vol. 190, No. 2, 2003, pp. 419–458. https://doi.org/https://doi.org/10.1016/S0021-9991(03)00282-1, URL https://www.sciencedirect.com/science/article/pii/S0021999103002821.

[39] Shukla, R. K., Tatineni, M., and Zhong, X., "Very high-order compact finite difference schemes on non-uniform grids for incompressible Navier–Stokes equations," *Journal of Computational Physics*, Vol. 224, No. 2, 2007, pp. 1064–1094. https://doi.org/https://doi.org/10.1016/j.jcp.2006.11.007, URL https://www.sciencedirect.com/science/article/pii/S0021999106005663.

[40] Mortensen, C. H., and Zhong, X., "Real-Gas and Surface-Ablation Effects on Hypersonic Boundary-Layer Instability over a Blunt Cone," *AIAA Journal*, Vol. 54, No. 3, 2016, pp. 980–998. https://doi.org/10.2514/1.J054404, URL https://doi.org/10.2514/1.J054404.

[41] Forgoston, E., and Tumin, A., "Initial-value problem for three-dimensional disturbances in a compressible boundary layer," *Physics of Fluids*, Vol. 17, No. 8, 2005, p. 084106. https://doi.org/10.1063/1.2013261, URL https://doi.org/10.1063/1.2013261.

[42] Kosloff, D., and Tal-Ezer, H., "A Modified Chebyshev Pseudospectral Method with an O(N-1) Time Step Restriction," *Journal of Computational Physics*, Vol. 104, No. 2, 1993, pp. 457–469. https://doi.org/https://doi.org/10.1006/jcph.1993.1044, URL https://www.sciencedirect.com/science/article/pii/S0021999183710442.

[43] Brent, R. P., *Algorithms for minimization without derivatives*, Courier Corporation, 2013.

[44] He, S., and Zhong, X., *Numerical Study of the Receptivity of a Blunt Cone to Freestream Pulse Disturbances in Hypersonic Flow*, AIAA, 2021. https://doi.org/10.2514/6.2021-2887, URL https://arc.aiaa.org/doi/abs/10.2514/6.2021-2887.

[45] Fedorov, A., and Khokhlov, A., "Prehistory of Instability in a Hypersonic Boundary Layer," *Theoretical and Computational Fluid Dynamics*, Vol. 14, 2001, pp. 359–375. https://doi.org/10.1007/s001620100038.

[46] Tumin, A., *Nonparallel Flow Effects on Roughness-Induced Perturbations in Boundary Layers*, AIAA, 2008. https://doi.org/10.2514/6.2008-504, URL https://arc.aiaa.org/doi/abs/10.2514/6.2008-504.

[47] Herbert, T., "PARABOLIZED STABILITY EQUATIONS," *Annual Review of Fluid Mechanics*, Vol. 29, No. 1, 1997, pp. 245–283. https://doi.org/10.1146/annurev.fluid.29.1.245, URL https://doi.org/10.1146/annurev.fluid.29.1.245.